Title

Exploring a Variable-Resolution Approach for Simulating Regional Climate in the Rocky Mountain Region Using the VR-CESM

Journal

Journal of Geophysical Research: Atmospheres, 122(20)

ISSN

2169-897X

Authors

Wu, Chenglai
Liu, Xiaohong
Lin, Zhaohui
et al.

Publication Date

2017-10-27

DOI

10.1002/2017jd027008

Peer reviewed

AGU PUBLICATIONS

JGR

Journal of Geophysical Research: Atmospheres

RESEARCH ARTICLE
10.1002/2017JD027008

Key Points:
- Variable-resolution CESM is able to accurately simulate the key climatological variables as well as their seasonality in the Rocky Mountains
- VR-CESM reproduces the seasonal evolution of snowpack with the timing of SWE peak (around early-middle April) close to the observations
- VR-CESM captures the observed occurrence frequency of heavy precipitation and rain-on-snow (ROS) events

Supporting Information:
- Supporting Information S1

Correspondence to:
X. Liu,
xliu6@uwyo.edu

Citation:
Wu, C., Liu, X., Lin, Z., Rhoades, A. M., Ullrich, P. A., Zarzycki, C. M., … Rahimi-Esfarjani, S. R. (2017). Exploring a variable-resolution approach for simulating regional climate in the Rocky Mountain region using the VR-CESM. *Journal of Geophysical Research: Atmospheres*, *122*, 10,939–10,965. https://doi.org/10.1002/2017JD027008

Received 21 APR 2017
Accepted 3 OCT 2017
Accepted article online 10 OCT 2017
Published online 28 OCT 2017

Exploring a Variable-Resolution Approach for Simulating Regional Climate in the Rocky Mountain Region Using the VR-CESM

Chenglai Wu[1,2], Xiaohong Liu[1], Zhaohui Lin[2,3], Alan M. Rhoades[4], Paul A. Ullrich[4], Colin M. Zarzycki[5], Zheng Lu[1], and Stefan R. Rahimi-Esfarjani[1]

[1]Department of Atmospheric Science, University of Wyoming, Laramie, WY, USA, [2]International Center for Climate and Environment Sciences, Institute of Atmospheric Physics, Chinese Academy of Sciences, Beijing, China, [3]University of Chinese Academy of Sciences, Beijing, China, [4]Department of Land, Air and Water Resources, University of California, Davis, CA, USA, [5]National Center for Atmospheric Research, Boulder, CO, USA

Abstract The reliability of climate simulations and projections, particularly in the regions with complex terrains, is greatly limited by the model resolution. In this study we evaluate the variable-resolution Community Earth System Model (VR-CESM) with a high-resolution (0.125°) refinement over the Rocky Mountain region. The VR-CESM results are compared with observations, as well as CESM simulation at a quasi-uniform 1° resolution (UNIF) and Canadian Regional Climate Model version 5 (CRCM5) simulation at a 0.11° resolution. We find that VR-CESM is effective at capturing the observed spatial patterns of temperature, precipitation, and snowpack in the Rocky Mountains with the performance comparable to CRCM5, while UNIF is unable to do so. VR-CESM and CRCM5 simulate better the seasonal variations of precipitation than UNIF, although VR-CESM still overestimates winter precipitation whereas CRCM5 and UNIF underestimate it. All simulations distribute more winter precipitation along the windward (west) flanks of mountain ridges with the greatest overestimation in VR-CESM. VR-CESM simulates much greater snow water equivalent peaks than CRCM5 and UNIF, although the peaks are still 10–40% less than observations. Moreover, the frequency of heavy precipitation events (daily precipitation $\geq$ 25 mm) in VR-CESM and CRCM5 is comparable to observations, whereas the same events in UNIF are an order of magnitude less frequent. In addition, VR-CESM captures the observed occurrence frequency and seasonal variation of rain-on-snow days and performs better than UNIF and CRCM5. These results demonstrate the VR-CESM's capability in regional climate modeling over the mountainous regions and its promising applications for climate change studies.

1. Introduction

The complex climate over the western United States is shaped by its unique geography under the influence of large-scale circulations (Leung et al., 2003). In this region, a diversity of regional-scale climatological gradients have been noted, from near the Pacific coast to interior mountains and from north to south, such as those gradients in precipitation amounts (Leung et al., 2003), seasonal cycles of precipitation (Hsu & Wallace, 1976), and partitioning of precipitation into rain and snow (Serreze et al., 1999). The need for high model fidelity at the fine spatial scales of these features has made climate modeling in this region very challenging. Moreover, not only is the western United States vulnerable to both natural climate variability and anthropogenic climate change, but the impacts of climate change may depend on topographical features such as elevation, slope, and orientation (Pederson et al., 2011; Rasmussen et al., 2011; Rhoades et al., 2017). In particular, in the inland western United States, the Rocky Mountains' snowpack is a primary source of water (Serreze et al., 1999). Snowfall, snow accumulation, and snow melt exhibit large interannual variations. They are also very sensitive to climate change. In the context of climate change, both temperature and precipitation may experience changes, which will impact the partitioning of total precipitation into snowfall and rainfall, as well as snow melt. Because of the great importance of water resources to human society and economic development, a major concern is how the character of regional climate and water resources will change in the future in the Rocky Mountain region. In addition, extreme precipitation, snow melt, and rain-on-snow events may result in river flooding hazards in the mountainous region, which may be influenced by future climate change (Berghuijs et al., 2016). Therefore, reliable regional climate information in the Rocky Mountain region is needed not only for the scientific understanding of regional climate change but also for applications in extreme weather vulnerability and impact assessments.

Global climate models (GCMs) have been widely used in the study of past and future climate and its underlying mechanisms. However, the performance of climate models is limited by the model resolution and the complexity of the subgrid-scale physics (e.g., Flato et al., 2013; National Research Council, 2012; Slingo et al., 2009). Model resolution is constrained by the rapid increase of computational costs associated with resolution and representation of sophisticated physics/chemistry, which prevents widespread application of (uniform) high-resolution GCMs despite the large increases in computational power over the past several decades (Haarsma et al., 2016). Consequently, two common approaches for high-resolution modeling have been generally employed. First, one approach is to use regional climate models (RCMs), forced at lateral boundaries by GCMs or reanalysis data (e.g., Christensen et al., 2013; Leung & Qian, 2003; Lucas-Picher et al., 2017; Singh et al., 2013; Walker & Diffenbaugh, 2009; Wehner, 2010, 2013). This approach is commonly referred to as dynamical downscaling. Depending on the sizes of model subdomains, required integration time, and available resources, horizontal resolutions of 1–30 km can be attained. However, this downscaling approach introduces inconsistencies in the physics and dynamics used in the global models (or reanalysis product) serving to drive RCMs and in the regional models (Laprise et al., 2008; Warner et al., 1997). Another approach is the use of variable-resolution GCMs (VR-GCMs) (e.g., Fox-Rabinovitz et al., 2006; Harris & Lin, 2013, 2014; Sakaguchi et al., 2015; Walko & Avissar, 2011; Zarzycki, Jablonowski et al., 2014). In this case, the model defines a high-resolution region similar to RCMs and simulates both the global and regional domains simultaneously, with a two-way flow of mass and energy. This preserves consistent physics in different regions and conserves air mass and energy globally, while keeping the computational cost relatively low compared with globally uniform high-resolution simulations.

Variable-resolution models have been used in climate modeling since the early to mid-1990s (e.g., Déqué & Piedelievre, 1995; Fox-Rabinovitz et al., 1997, 2006). Early studies used stretched grid techniques to increase the horizontal resolution in a specific region. However, this technique also tends to lead to an excessively coarse mesh that is antipodal to the refinement region, which can negatively impact the fidelity of the large-scale circulation. With the development of atmospheric numerical techniques, VR-GCMs using unstructured grids have been developed in recent years (e.g., Harris & Lin, 2013, 2014; Sakaguchi et al., 2015; Walko & Avissar, 2011; Zarzycki, Jablonowski et al., 2014). These unstructured grids can transit smoothly from quasi-uniform global grids to a regionally refined domain. Therefore, fine-scale features in the regional domain may develop, propagate, and interact with the coarser global regions to provide a more unified dynamic framework for the interactions of global and regional scales. VR-GCMs have also shown improved results in the simulations of tropical storms and orographic precipitation (e.g., Harris & Lin, 2014; Sakaguchi et al., 2015; Zarzycki & Jablonowski, 2014; Zarzycki et al., 2015).

Recently, a variable-resolution version of Community Earth System Model (VR-CESM) has been developed (Zarzycki, Jablonowski et al., 2014; Zarzycki, Levy et al., 2014). With a high-resolution refinement region placed over the North Atlantic hurricane basin, VR-CESM showed significant improvement in the simulations of Atlantic tropical storms (Zarzycki, Jablonowski et al., 2014) and orographically forced flow in the Americas (Zarzycki et al., 2015). The model was also used to simulate the regional climate in California and along the Sierra Nevada mountain range (Huang et al., 2016; Rhoades et al., 2016). The results demonstrate that VR-CESM is skillful in reproducing the spatial patterns and the seasonal evolution of temperature, precipitation, and snowpack, with biases generally comparable in magnitude, but different in character, to those produced by the regional Weather Research and Forecast (WRF) model at a similar horizontal resolution. The different characters of the simulated biases between VR-CESM and WRF indicate the underlying structural uncertainties in climate modeling. For instance, biases may be in similar magnitudes but appear in different seasons and regions, have opposite signs, or will be smaller in one metric (e.g., average, minimum, or maximum of temperature) but larger in another. Furthermore, VR-CESM was used to assess the impacts of climate change on western United States hydroclimatology under a business-as-usual emissions scenario (Representative Concentration Pathway 8.5, RCP8.5) (Huang & Ullrich, 2017; Rhoades et al., 2017). As shown in these studies, VR-CESM can greatly increase the reliability of climate simulations and projections in topographically complex regions.

Previous studies using VR-CESM mainly focus on the Atlantic Ocean and the coastal regions of United States. In this study we use VR-CESM to simulate the regional climate in the Rocky Mountain region, which covers much of the inland of the western United States. The VR-CESM simulation is compared with a quasi-uniform coarse resolution CESM simulation, the Canadian Regional Climate Model version 5 (CRCM5) simulation, and

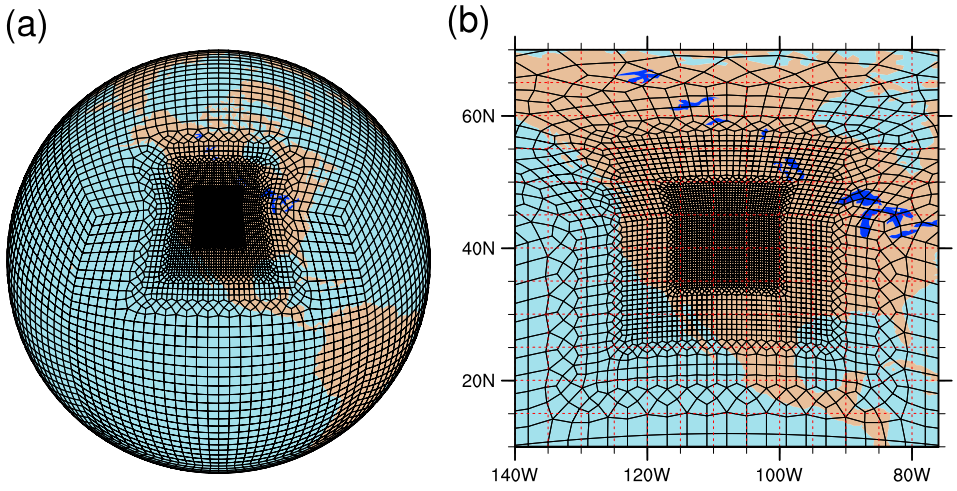

Figure 1. (a) Model mesh for the variable resolution grid (uniform 1° with refined 0.125° over the Rocky Mountain region) used in VR-CESM. (b) As in Figure 1a but zoom in to depict the transitions from the global quasi-1° resolution mesh to 0.125° resolution mesh through two layers of refinement (0.5° and 0.25°). Note that each grid element shown contains an additional 3 × 3 collocation grid cells.

various observations. The purpose of this study is to assess the performance of VR-CESM in the simulation of (1) important climatological quantities (temperature, precipitation, and snowpack), including their spatial distributions and seasonality, and (2) the occurrence of heavy precipitation and rain-on-snow (ROS) events. Such an assessment is needed to understand how modern modeling techniques can be used to improve modeled climatology in regions of complex terrain, and how the model can be used to study the past and future climate change in the Rocky Mountain region.

The remainder of the paper is organized as follows. In section 2, we introduce the model and experimental design. Section 3 describes the observation data used for model evaluation. Section 4 presents the simulation results and evaluations of spatial patterns and seasonal evolutions of temperature, precipitation, and snowpack, along with the comparison of the frequency of daily precipitation rate and ROS days with observations. A discussion of model biases follows in section 5. Conclusions are given in section 6.

2. Model and Experimental Design

VR-CESM is a version of CESM with variable resolution compatibility. CESM is a state-of-the-art Earth system modeling framework, allowing for the investigation of the Earth system across multiple time and space scales (Hurrell et al., 2013). CESM version 1.2.0 uses the Community Atmosphere Model version 5 (CAM5) for the atmosphere component (Neale et al., 2010). Variable-resolution support requires the use of CAM5 with the Spectral Element (SE) dynamic core (CAM-SE) (Zarzycki, Levy et al., 2014; Zarzycki, Jablonowski et al., 2014). The SE dynamic core uses a continuous Galerkin spectral finite-element method designed for fully unstructured quadrilateral meshes and has demonstrated near-optimal (close to linear) parallel scalability on tens of thousands of cores (Dennis et al., 2012). This enables the model to run efficiently on the decadal to multidecadal time scales. For the land component, CESM uses the Community Land Model version 4 with satellite phenology (CLM4-SP) (Oleson et al., 2010).

CESM includes advanced physics for CAM5 (Neale et al., 2010) and CLM4-SP (Oleson et al., 2010). The CAM5 physics suite includes shallow convection (Park & Bretherton, 2009), deep convection (Richter & Rasch, 2008; Zhang & McFarlane, 1995), cloud microphysics (Morrison & Gettelman, 2008) and macrophysics (Park et al., 2014), radiation (Iacono et al., 2008), and aerosols (Liu et al., 2012). CLM4-SP physics include a suite of parameterizations for land-atmosphere exchanges. In particular, snowpack is explicitly represented by a snow model coupled with the Snow, Ice, and Aerosol Radiation model for snow-aerosol-climate interactions (Flanner et al., 2007).

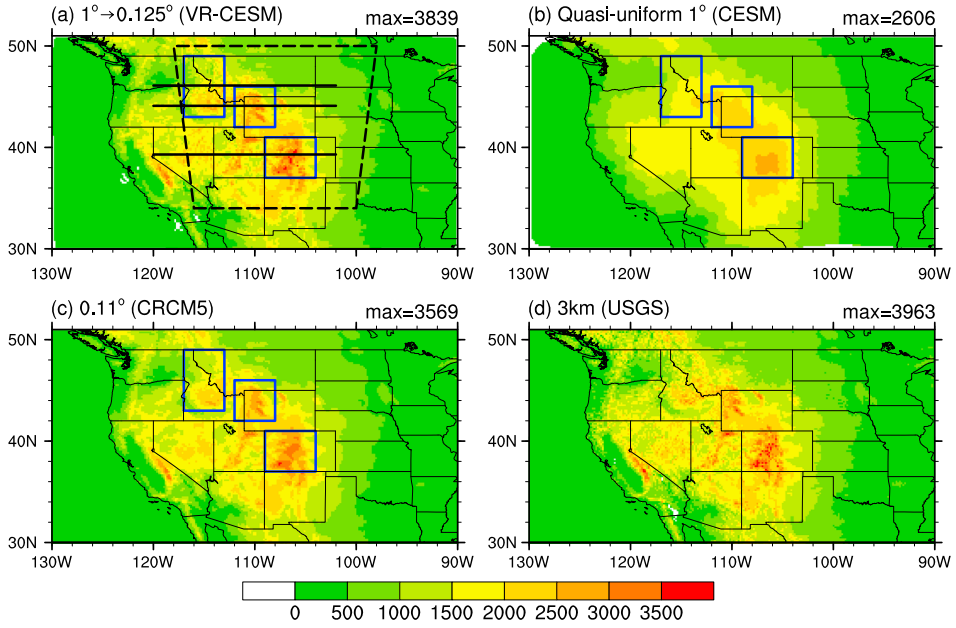

Figure 2. Terrain height (m) in the western U.S. for (a) variable resolution used in VR-CESM, (b) quasi-uniform 1° in CESM, (c) 0.11° in CRCM5, and (d) ~3 km resolution generated from United States Geological Survey (USGS) 30 s (~1 km) data (Lauritzen et al., 2015). The maximum terrain height in the Rocky Mountains is given in the right top of each plot. Note that the refined region at a resolution of 0.125° is surrounded by dashed lines in Figure 2a. The three blue rectangles denote the Northern Rockies, Greater Yellowstone region, and Southern Rockies for the analysis in this study. The three black lines in Figure 2a indicate the three latitudes (46.1°N, 44.1°N, and 39.3°N) transecting these three regions, respectively.

For this study, a variable-resolution grid has been generated by the open-source software package SQuadGen (Guba et al., 2014; Ullrich, 2014). SQuadGen uses paving for the generation of the variable-resolution grid and spring dynamics for the smoothing of the transitional regions between various grid resolutions. As shown in Figure 1, the resolution transitions from quasi-uniform 1° to refined 0.125° over the Rocky Mountain region (a factor of 8 times refinement), with two intermediate transitions at resolutions of 0.5° and 0.25°. CLM4-SP is run at the same resolutions as CAM-SE to better represent the snow hydrology associated with the variability of terrain. Note that, in accordance with the SE method, each mesh element shown in Figure 1 contains 3 × 3 collocation grid cells (i.e., each element is further discretized horizontally into 3 × 3 grids to solve the dynamic equations for SE) that define the actual grid resolution of the model. Although it is desirable to extend the refined region (~0.125°) to the whole western United States, this would greatly increase the number of grid cells in the simulations and impact computational costs. For the grid we are using, the resolution over the remainder of the western United States is still reasonably high (~0.25°).

A topography data set for the variable-resolution grid is generated by the National Center for Atmospheric Research (NCAR) global model topography generation software called NCAR_Topo (v1.0) (Lauritzen et al., 2015). This data set is remapped from the intermediate data on ~3 km resolution cubed-sphere grid, and this intermediate data are generated from the United States Geological Survey (USGS) 30 s (~1 km) data (Lauritzen et al., 2015). No further smoothing is applied to the data set, allowing us to preserve more detailed features of the terrain. Note that previous studies have shown that different levels of smoothing in topography can affect the simulated climatology in mountainous regions (e.g., Rhoades et al., 2016). However, no rigorous testing has been performed to determine the minimal level of smoothing needed (Lauritzen et al., 2015; Rhoades et al., 2016). The sensitivity of our simulation results to the smoothing of topography will be analyzed in a separate study. Figure 2 shows the comparison of topography adopted in the uniform 1° grid and in the variable-resolution grid. It is clear that the coarse 1° grid cannot resolve the rapidly varying topography in the Rocky Mountain region, whereas the refined 0.125° grid in VR-CESM produces a more physically consistent representation of the mountain ridges and valleys. The maximum elevation of the Rocky Mountains for variable resolution and uniform 1° resolution is 3,839 m and 2,606 m, respectively, compared to 3,963 m from the USGS 3 km data.

Table 1
Model Grids and Time Steps for CAM-SE in Uniform 1° CESM (UNIF) and VR-CESM

Model	Resolution	Number of elements[a]	Physics time step (s)	Dynamic time step (s)
Uniform 1° CESM (UNIF)	~1°	5,400	1,800	90
VR-CESM[b]	1°→0.125°	8,996	900	9

[a]Each element contains 3 × 3 collocation grid cells that define the actual grid resolution of the model (Dennis et al., 2012). [b]VR-CESM uses a variable resolution grid that transits from global quasi-uniform 1° to refined high resolution (0.125°) over the Rocky Mountain region (section 2 and Figure 1).

Following the Atmospheric Model Intercomparison Project protocols (Gates, 1992), the model is run in the coupled land-atmosphere mode with observed 1° × 1° sea surface temperatures and sea ice coverage prescribed at monthly intervals (Hurrell et al., 2008). Historical greenhouse gas concentrations and anthropogenic aerosol and precursor gas emissions are prescribed (Lamarque et al., 2010). In addition to the VR-CESM simulation, we also performed a CESM simulation with a quasi-uniform 1° grid (referred to as UNIF hereafter) to assess the performance of VR-CESM compared to a more traditional GCM resolution. The number of vertical levels is equal to 30 for both simulations. As shown in Table 1, the number of grid elements increases from 5,400 (quasi-uniform 1°) to 8,996 (VR-CESM) due to the increase of horizontal model resolution.

The dynamics time step in VR-CESM is reduced by 10 times (i.e., 9 s in VR-CESM versus 90 s in UNIF) to satisfy the Courant-Friedrichs-Lewy stability condition for the finest scale in the variable-resolution grid. The physics time step is set differently, i.e., 30 min for UNIF and 15 min for VR-CESM. The physics time step of 15 min for VR-CESM is consistent with a previous study using CESM/CAM-SE quasi-uniform at 0.125° resolution (Dennis et al., 2012). Note that the physics time step for VR-CESM is reduced to allow for a smaller number of dynamics time steps within a physics time step, which can reduce the imbalance between physics and dynamics. In addition, the parameter values of CAM5-SE and CLM4-SP physics parameterizations in VR-CESM are the same as those in the UNIF. As a result of reduced physics and dynamics time steps and increased number of elements, the computational cost is increased by a factor of 8 in VR-CESM compared to UNIF. However, this is still very economical considering that CESM with a globally uniform 0.125° grid (345,600 elements) using the same physics and dynamic time steps as VR-CESM would be approximately 38 times the computational cost of VR-CESM. About 1.73 simulated years per day for VR-CESM was observed with 1800 cores of the NCAR-Wyoming Supercomputer Center's Yellowstone supercomputer.

Both VR-CESM and UNIF simulations are run from January 1979 to December 2005, and we analyze the results over a 25 year time frame (from 1981 to 2005) in accordance with the period of available observations (section 3). The first two years (1979–1980) can be regarded as a spin-up period. Note that typically CLM4 needs a longer period to spin-up, but here CLM4 initial conditions are from historical CESM simulations (i.e., from 1850 to present day) and are at reasonably balanced states. For the evaluation of regional climate statistics, we mainly focus on the three regions in the Rocky Mountain region, as shown in Figure 2. These three regions are the Northern Rockies (113–117°W, 43–49°N), the Greater Yellowstone region (108–112°W, 42–46°N), and the Southern Rockies (104–109°W, 37–41°N), respectively.

To demonstrate the performance of VR-CESM in comparison to the RCM downscaling approach, VR-CESM simulation is also compared to CRCM5 simulation from the North American Coordinated Regional Downscaling Experiment (NA-CORDEX) (Giorgi et al., 2009). CRCM5 is a state-of-the-art RCM (Martynov et al., 2013; Šeparović et al., 2013), developed at the Centre Pour l' Étude et la Simulation du Climat à l'Échelle Régionale at the Université du Québec à Montréal (UQAM). CRCM5 is based on a limited-area version of the Global Environment Multiscale (GEM) model (Zadra et al., 2008). GEM is a grid point model based on a two-time level semi-Lagrangian, (quasi) fully implicit time discretization scheme. GEM includes a terrain-following vertical coordinate based on a hydrostatic pressure and a horizontal discretization on a rotated latitude-longitude, Arakawa C grid. The nesting technique employs the outermost 10-point "halo" zone along the lateral boundaries for the semi-Lagrangian interpolation and the next 10-point sponge zone for a gradual relaxation of the driving data. For the land surface, CRCM5 uses the Canadian Land-Surface Scheme version 3.5 (Verseghy, 2009), allowing for a flexible number of layers and depth with snow explicitly treated. The detailed description of CRCM5 including the dynamic formulation and physical

parameterizations can be found in Zadra et al. (2008), Martynov et al. (2013), Šeparović et al. (2013), and Lucas-Picher et al. (2017).

CRCM5 has contributed to the NA-CORDEX project to simulate the current and future climate in the whole North America (Martynov et al., 2013; Šeparović et al., 2013). Here we use the CRCM5 simulation at a horizontal resolution of 0.11°, which is comparable to the resolution of 0.125° in VR-CESM. The number of vertical levels is 58, and the time step is 5 min. The domain covers the whole North America with 675 × 660 grid cells. The CRCM5 simulation was performed from 1979 to 2014 with the lateral boundaries (wind, temperature, specific humidity, and surface pressure) provided every 6 h by European Centre for Medium-Range Weather Forecasts' ERA-Interim reanalysis (Dee et al., 2011). SST and sea ice fraction from ERA-Interim are prescribed once per year. Note that although various models with different resolutions (0.44° or 50 km, 0.22° or 25 km, 0.11°) are used in NA-CORDEX (https://na-cordex.org/simulations-modeling-group), only CRCM5 is performed at the highest resolution of 0.11° and thus is used in this study. The simulation during the period of 1981–2005 is used for the comparison, and regional statistics is also made in the three regions (Northern Rockies, Greater Yellowstone region, and Southern Rockies). Note that CRCM5 adopts a smoother topography than VR-CESM, with the maximum elevation of Rocky Mountains about 3,569 m (Figure 2).

3. Observational and Reanalysis Data

For evaluation of the simulated climate in mountainous regions, we employ daily observations from the Snow Telemetry (SNOTEL) network, operated by the Natural Resources Conservation Service (NRCS) branch of U.S. Department of Agriculture. SNOTEL has been widely used by previous studies in characterizing the climate in the Rocky Mountains (e.g., Serreze et al., 1999) and in evaluating the performance of climate models (e.g., Rasmussen et al., 2011). This data set contains daily snow water equivalent (SWE), precipitation, and mean, maximum, and minimum temperature (hereafter referred to as T_{mean}, T_{max}, and T_{min}, respectively), as recorded by automated sensors from over 800 mountain sites. SWE is defined as the amount of water contained within the snowpack, measured by kg m^{-2} that is equivalent to millimeter after dividing the density of water (1,000 kg m^{-3}). Although SNOTEL observations date back to the 1960s, most records began in the early 1980s (Serreze et al., 1999). A major limitation in the SNOTEL observation is undercatch of precipitation (i.e., precipitation caught by the precipitation gauges is lower than real precipitation), which may occur due to the influence of wind (Groisman & Easterling, 1994; Yang et al., 1998). Yang et al. (1998) reported that undercatch can account for several tens of percent of real precipitation when wind speeds are larger than 2 m s^{-1}. Lighter and slower falling snow hydrometers are more prone to deflection by wind-induced turbulence around the gauge, making snowfall measurements more susceptible to these errors than those of rainfall (Rasmussen et al., 2012). Therefore, a comparison of simulated precipitation with SNOTEL precipitation may be affected by the observation errors. Another relevant consideration is that SNOTEL only records daily precipitation that is at least 0.1 inch (2.54 mm). In contrast, the model captures all precipitation.

To derive a climatology of SNOTEL observations for the model evaluation, we select only stations with adequate observations during 1981–2005 as described below. Namely, for SWE and precipitation, we use the stations where observations are available for more than 20 years. In total 70, 59, and 48 stations were selected for SWE and precipitation in the Northern Rockies, Greater Yellowstone region, and Southern Rockies, respectively. For temperature, the observational record generally begins in the late 1980s or later, and we only select the stations with more than 15 year observations for temperature, which leads to 56, 61, and 50 stations in the Northern Rockies, Greater Yellowstone region, and Southern Rockies, respectively. For model evaluation, results from the model grids are interpolated to the SNOTEL stations using the inverse distance weighted interpolation within a 3-D interpolation package called Dsgrid. Although terrain characteristics (e.g., terrain height, slope, and aspect) can lead to large spatial variations of snowpack in the mountains, knowledge of relationships between snowpack and terrain characteristics is limited and these relationships are not yet available for consideration in the interpolation. After the interpolation, regional statistics (e.g., means, standard deviations, and frequency distributions of daily precipitation) are then calculated for both the simulations and observations.

We also calculate the number of ROS days at SNOTEL stations for both simulations and observations. A ROS day at a station is defined if a notable amount of precipitation (i.e., $>$10 mm) falls during the day and SWE is reduced on the consecutive day, following Guan et al. (2016) that also calculated ROS events at SNOTEL

stations. A threshold of 1 mm for SWE change is required to define ROS days, assuming SWE change due to other factors such as the sublimation of snow is small. A similar approach was also used in McCabe et al. (2007), who noted that some ROS events may not result in the reduction of SWE. However, our focus in this study is on ROS events that could potentially have a hydrologic effect and thus only ROS events that resulted in a decrease in SWE are analyzed. Note that some observations are unavailable during the water year (defined from 1 October to 30 September in the consecutive year) from 1981 to 1985. Thus, we only select the stations with 20 year consecutive observations during water year 1986–2005 and calculate the number of ROS days during 1986–2005 for simulations and observations. In total there are 50, 57, and 51 selected stations in Northern Rockies, Greater Yellowstone region, and Southern Rockies, respectively,

For evaluation of the simulated spatial distributions, we also use the 4 km gridded data set from the Parameter-elevation Regressions on Independent Slopes Model (PRISM) (Daly et al., 2008). This data set is provided by the PRISM Climate Group at Oregon State University. PRISM applies a factor-weighted climate-elevation regression to interpolate the observations at surface stations to each digital elevation model cell. Although many factors are considered, PRISM assumes that elevation is the most important factor that influences the precipitation distribution (Daly et al., 2008). The data set includes daily precipitation (Pr) and daily T_{mean}, T_{max}, and T_{min}. In this data set, T_{mean} is derived from the mean of T_{max} and T_{min}. The historical time series data start from January 1981 and are used to evaluate the modeled spatial distributions of temperature and precipitation for 1981–2005. Note that SNOTEL and PRISM are not independent data sets: SNOTEL in situ measurements are assimilated in PRISM, and thus the PRISM data set may incorporate errors from SNOTEL measurements. For quantitative comparisons, the spatial correlation (SCORR) and root-mean-square error (RMSE) between the simulations and PRISM observations are calculated by mapping the simulation results to the PRISM grids using the bilinear interpolation.

As the SNOTEL network only provides observations at mountain stations, to evaluate the spatial patterns of snow cover, we also use the monthly Level-3 (L3) global 0.05° × 0.05° snow cover fraction (SCF, defined as the fraction of surface area covered by snow) from the Moderate Resolution Imaging Spectroradiometer (MODIS) remote sensing observations (Hall et al., 2006). The data set appears to reasonably represent snow cover when compared with other data sets, and the reported accuracy is in the range of 88% to 93% (Hall et al., 2006; Hall & Riggs, 2007). The most frequent errors are due to snow/cloud discrimination problems, but improvements in the MODIS cloud mask have been made to make the data set useful in regional and global studies (Hall & Riggs, 2007). Both MODIS/Aqua and MODIS/Terra data sets are used to account for the observational uncertainty. We use MODIS data from December 2002 to November 2015 (13 years), when both MODIS/Aqua and MODIS/Terra data sets are available. Although the observation period does not exactly match the simulation period, a 13 year mean SCF can provide the mean state of snow cover and thus can be used for the model evaluation from a climatological perspective. SCORR and RMSE between the simulations and MODIS observations are calculated by remapping the simulation results to 0.05° × 0.05° grids using the bilinear interpolation.

To identify biases in meteorological conditions that are critical to understanding regional climate in the Rocky Mountains, we also compare the simulated meteorology with National Centers for Environmental Prediction's (NCEP) North American Regional Reanalysis (NARR; Mesinger et al., 2006). NARR is provided at a horizontal resolution of 32 km with 29 pressure levels from 1979 to present. NARR is generated using the NCEP Eta (32 km horizontal resolution with 45 vertical levels) together with the Regional Data Assimilated System (RDAS). The RDAS takes in, or assimilates, a great amount of observational data to produce a long-term picture of weather over North America. The monthly zonal winds, temperature, and horizontal (including zonal and meridional) water vapor flux averaged during the period of 1981–2005 are used here. Zonal (meridional) water vapor flux is calculated from 3-hourly specific humidity and zonal (meridional) winds, and the flux is then averaged to obtain the monthly mean. To examine the winter storm activity, we also calculate the root-mean-square (RMS) of band-pass filtered 500 hPa geopotential height at periods of 2.5–6 days following Blackmon (1976). The RMS of band-pass filtered 500 hPa geopotential height is a good indicator of storminess (Blackmon, 1976). It is calculated from 6-hourly 500 hPa geopotential height for each winter and is then averaged to obtain the winter mean during the period 1981–2005. For the comparison of simulations with NARR, both of them are interpolated linearly to a grid with a spatial resolution of 0.125°, and meteorology at the hybrid coordinate in CESM is interpolated linearly to the pressure levels as in NARR.

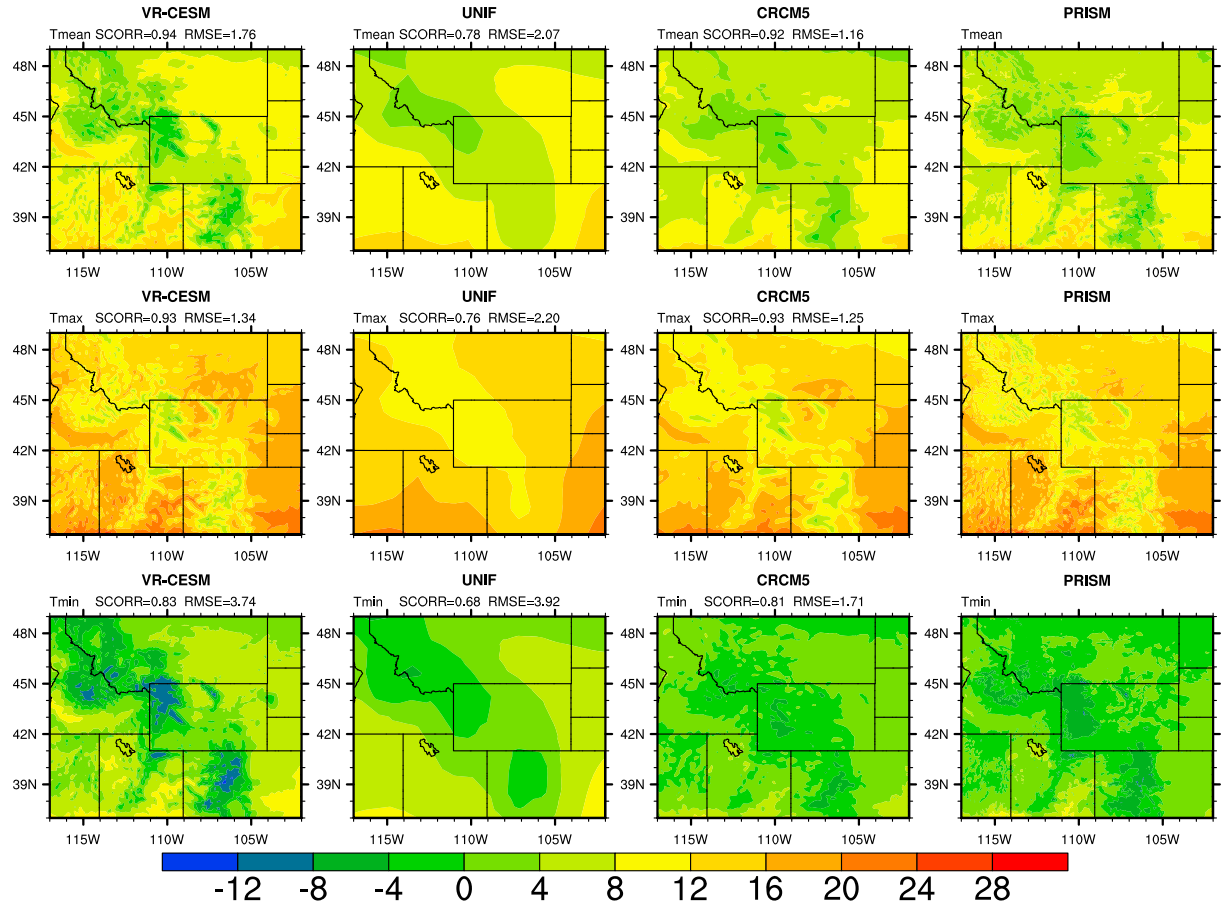

Figure 3. (top row) Annual mean, (middle row) mean daily maximum, and (bottom row) mean daily minimum surface air temperature (°C) from (first column) VR-CESM, (second column) UNIF, (third column) CRCM5, and (fourth column) PRISM observations. Also shown are the spatial correlation (SCORR) and root-mean-square-error (RMSE) between each simulation and PRISM observations across the whole region (37–49 °N, 102–117 °W).

4. Results

4.1. Spatial Patterns

4.1.1. Temperature

Figure 3 shows the spatial distribution of annual T_{mean}, T_{max}, and T_{min} during 1981–2005 from the VR-CESM, UNIF, and CRCM5 simulations and PRISM observations (differences between simulation and observation are shown in Figure S1 in the supporting information). SCORR and RMSE between simulation and observation across the whole region (37–49°N, 102–117°E) are also given in the figures. The observations show distinctly lower temperature in the mountains, and the spatial pattern of observed temperatures corresponds well with the topographic variation. Compared to observations, VR-CESM clearly captures the spatial distribution of temperature, with SCORR values between VR-CESM and observations of 0.94, 0.93, and 0.83 for T_{mean}, T_{max}, and T_{min}, respectively. UNIF only captures the largest-scale spatial patterns in these regions, with SCORR values between UNIF and observations all below 0.8. RMSE between UNIF and observations is also larger than that between VR-CESM and observations. Due to the more smoothed topography used in CRCM5, slightly smaller SCORR is found for CRCM5 compared to VR-CESM. However, RMSE between CRCM5 and observations is smaller (especially 2°C smaller for T_{min}) than that between VR-CESM and observations.

VR-CESM simulates reasonably well the magnitude of T_{max} with biases mostly within ±2°C. Larger T_{max} biases can be found over the Wind River Range (approximately from 43.4°N, 110.3°W in the northwest to 42.5°N, 108.9°W in the southeast) and the northwestern part of Northern Rockies, with the biases ranging from −2 to −6°C and from 2 to 4°C, respectively. However, VR-CESM produces T_{min} cold biases around −1°C to −6°C in the mountains, and as a result, VR-CESM simulates 0.5–4°C lower T_{mean} than observations.

Table 2
The Spatial Correlations (SCORR) of Temperature and Precipitation Between VR-CESM, UNIF, and CRCM5 Simulations and PRISM Observations

Annual/season	VR-CESM	UNIF	CRCM5
		T_{mean}	
Annual	0.94 (0.82–0.95)	0.78 (0.68–0.80)	0.92 (0.87–0.93)
Winter	0.90 (0.64–0.91)	0.84 (0.45–0.87)	0.82 (0.62–0.89)
Spring	0.93 (0.77–0.95)	0.72 (0.56–0.76)	0.91 (0.81–0.93)
Summer	0.93 (0.80–0.94)	0.75 (0.64–0.79)	0.94 (0.85–0.95)
Autumn	0.92 (0.77–0.94)	0.78 (0.67–0.82)	0.93 (0.88–0.94)
		T_{max}	
Annual	0.93 (0.81–0.94)	0.76 (0.61–0.80)	0.93 (0.90–0.93)
Winter	0.91 (0.61–0.91)	0.85 (0.39–0.88)	0.89 (0.71–0.92)
Spring	0.93 (0.73–0.93)	0.70 (0.46–0.75)	0.92 (0.85–0.93)
Summer	0.90 (0.70–0.93)	0.67 (0.38–0.71)	0.92 (0.84–0.94)
Autumn	0.94 (0.73–0.94)	0.77 (0.51–0.83)	0.94 (0.87–0.94)
		T_{min}	
Annual	0.83 (0.73–0.86)	0.68 (0.57–0.72)	0.81(0.73–0.83)
Winter	0.73 (0.46–0.78)	0.69 (0.29–0.78)	0.73 (0.61–0.82)
Spring	0.86 (0.73–0.86)	0.66 (0.57–0.72)	0.81 (0.73–0.83)
Summer	0.86 (0.67–0.89)	0.74 (0.53–0.75)	0.87 (0.67–0.83)
Autumn	0.77 (0.74–0.88)	0.64 (0.60–0.77)	0.84 (0.76–0.91)
		Precipitation	
Annual	0.75 (0.59–0.78)	0.56 (0.22–0.63)	0.83 (0.63–0.84)
Winter	0.80 (0.54–0.82)	0.70 (0.47–0.74)	0.87 (0.68–0.88)
Spring	0.70 (0.32–0.69)	0.49 (−0.08–0.60)	0.78 (0.23–0.82)
Summer	0.66 (0.12–0.73)	0.61 (0.18–0.71)	0.90 (0.22–0.87)
Autumn	0.73 (0.14–0.76)	0.58 (0.15–0.70)	0.82, (0.41–0.83)

Note. The range of SCORR values calculated for each year during 1981–2005 is given in parenthesis next to the value for the mean of 1981–2005.

Meanwhile, VR-CESM produces T_{min} warm biases around +2°C to +8°C in the plains, leading to 0.5–4°C warmer T_{mean} than observations there. These biases may in part result from the overestimation of SCF in VR-CESM (section 4.1.3). Overall, the RMSE for T_{min} simulated by VR-CESM is 3.74°C, which is about 2°C larger than for T_{mean} and T_{max}. For CRCM5, the magnitude of T_{max} biases is similar to that for VR-CESM except in the Wind River Range and the northwestern part of Northern Rockies where the T_{max} biases are smaller in CRCM5. Compared to T_{min} cold bias in the mountains in VR-CESM, T_{min} biases in CRCM5 are in similar magnitude but in an opposite sign (around +1°C to +6°C). However, CRCM5 produces much smaller T_{min} biases in the plains, leading to a smaller RMSE (1.71°C) compared to VR-CESM (3.74°C). Table 2 gives the SCORR for the mean of 1981–2005 and the range of SCORR for each year from 1981 to 2005. SCORRs differ by 0.1–0.3 year by year in VR-CESM and CRCM5. SCORRs for the mean of 1981–2005 are mostly at the upside of the range. The range of SCORRs in VR-CESM is slightly larger than that in CRCM5. This can be expected since CRCM5 is driven by the reanalysis from the lateral boundaries.

Note that the observed T_{min} varies less with elevation than the observed T_{max}, and VR-CESM simulates stronger variations of both T_{max} and T_{min} with elevation. In winter, extreme temperature inversions (i.e., a positive lapse rate of temperature with altitude) are observed in some cases in the mountain-valley regions at night (M. Doggett, personal communication, 2016). Events of this nature may offset the typically decreased temperature with elevation, leading to a weaker dependence of T_{min} (corresponding to nighttime lowest temperature) with elevation on average. The T_{min} cold biases with increasing elevation (compared to PRISM) may indicate that the model lacks the ability to simulate the large-scale (e.g., temperature advection and subsidence) to mesoscale conditions (e.g., downslope flow and accumulation of cold air) for these temperature inversions (Lareau et al., 2013). The spatial patterns of seasonal mean T_{mean}, T_{max}, and T_{min} are similar to those in annual results, except that compared to annual observation results, summer (June-July-August) observations show more pronounced variation of T_{min} with elevation, which is well captured by VR-CESM (Figures S2–S9). From the contribution of biases from all four seasons to annual mean biases, we can also find the annual cold (warm) biases in the mountains in VR-CESM (CRCM5) mainly emerges from the wintertime (summertime). This result will be further discussed in section 4.2.

4.1.2. Precipitation

Figure 4 shows the spatial distribution of annual and four seasonal mean precipitation from VR-CESM, UNIF, and CRCM5 simulations and PRISM observations. Differences between each simulation and observations are depicted in Figure 5. Driven by orographic uplift, observed precipitation is larger in the mountainous regions. Furthermore, most of the annual precipitation occurs in the cold season (October to May) (Figure 4, fourth column). Although UNIF produces precipitation amounts that are roughly comparable to observations, UNIF is unable to capture the fine-scale spatial structure of precipitation. As expected, 1° resolution is simply too coarse to resolve the topographic variability of the mountains (Figure 2). With a much higher resolution (0.125° and 0.11°), VR-CESM and CRCM5 resolve the fine-scale features of precipitation in the observations, with SCORR around 0.75 and 0.83, respectively, for the annual precipitation. Whereas precipitation simulated by CRCM5 is distributed slightly smoother than in observations, VR-CESM tends to produce some local peaks of precipitation that are larger than observations. This can explain the smaller SCORR for VR-CESM than for CRCM5. VR-CESM and CRCM5 also reproduce the magnitude of annual mean precipitation with positive biases (around 0.5–4 mm/d for VR-CESM and 0.5–2 mm/d for CRCM5) along the western side of Northern Rockies and Greater Yellowstone region. In particular, in winter, both VR-CESM and CRCM5 effectively capture the wintertime orographic precipitation, although it overestimates the precipitation rate in the western side of mountains. This overestimation is more pronounced in the Northern Rockies and Greater Yellowstone

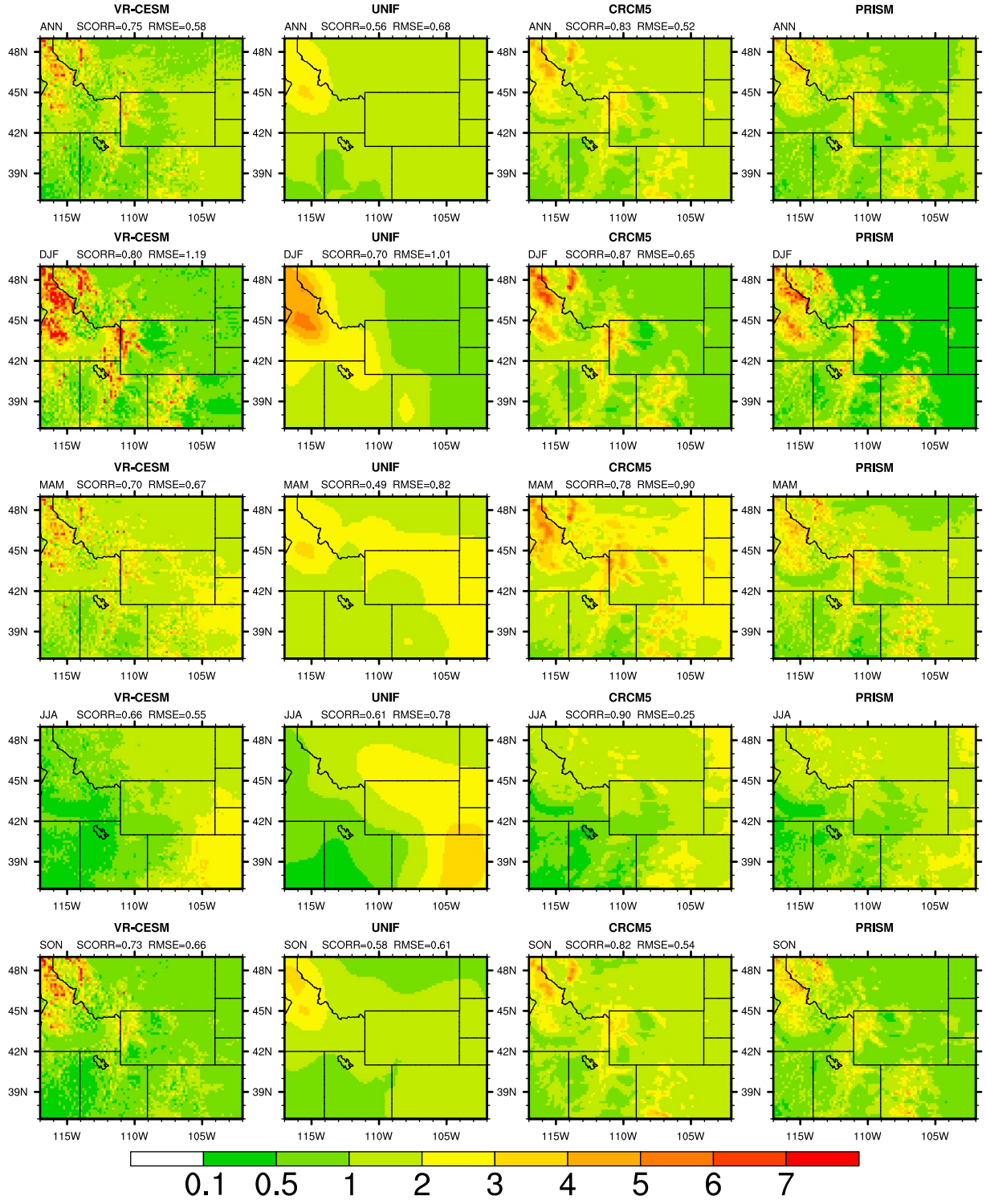

Figure 4. As in Figure 3 but for (first row) annual, (second row) winter, (third row) spring, (fourth row) summer, and (fifth row) autumn mean precipitation rate (mm/d).

region, and less so in the Southern Rockies. In spring, VR-CESM simulates drier conditions in the mountains, with a negative precipitation bias of 0.5–3 mm/d when compared to observations. On the other hand, CRCM5 produces larger precipitation by 0.5–3 mm/d in the Northern Rockies and Greater Yellowstone region. Along the eastern side of Rocky Mountains, CRCM5 also produces a precipitation bias of +0.5 to

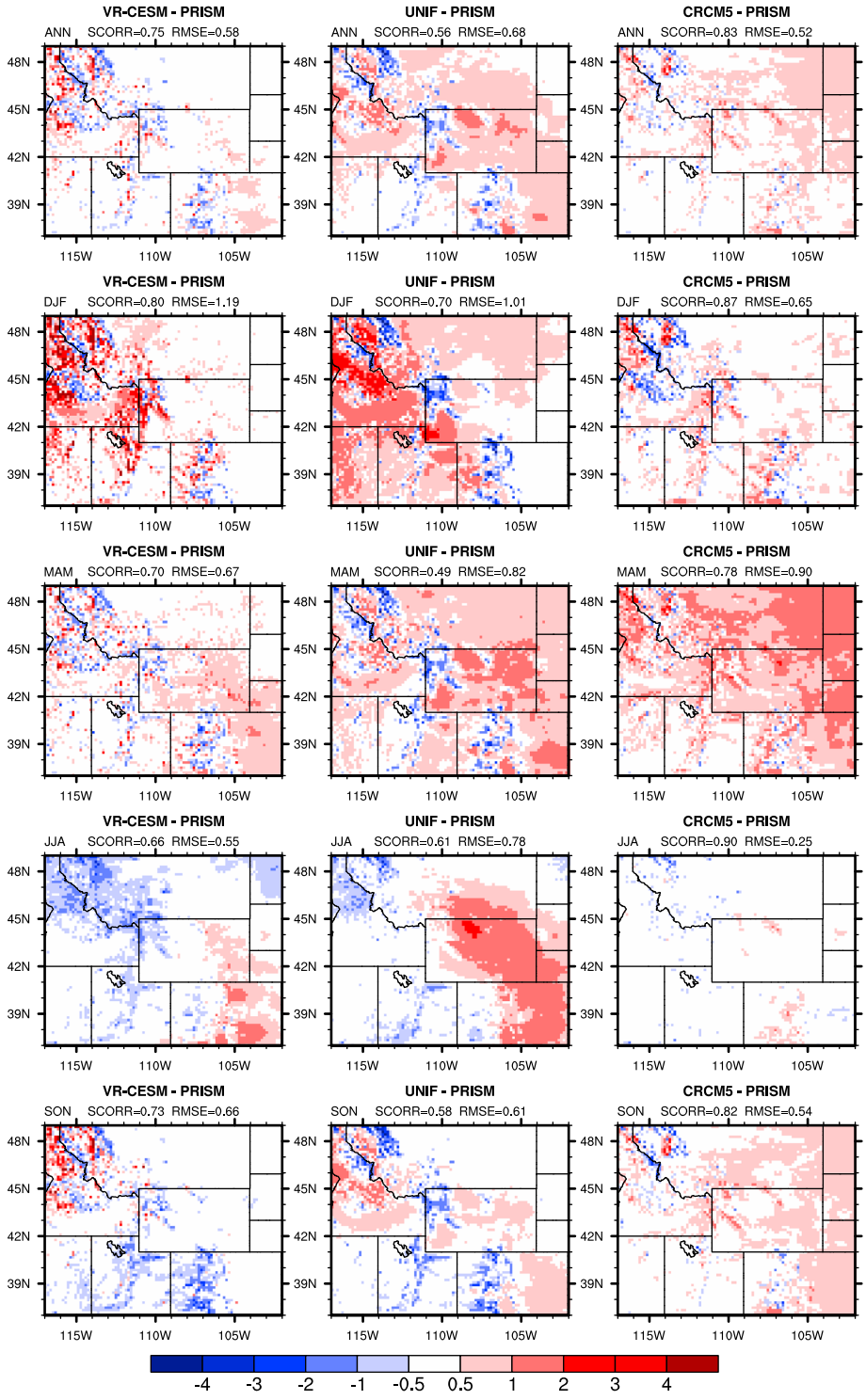

Figure 5. As in Figure 4 but for the difference between each simulation and PRISM observations.

+2 mm/d, which is much larger than VR-CESM, although biases of between 0 and +0.5 mm/d are also found in VR-CESM in this region.

In summer, both VR-CESM and UNIF simulate much less precipitation in the mountains than in winter, which is consistent with observations. VR-CESM captures the spatial variation of observed summer precipitation

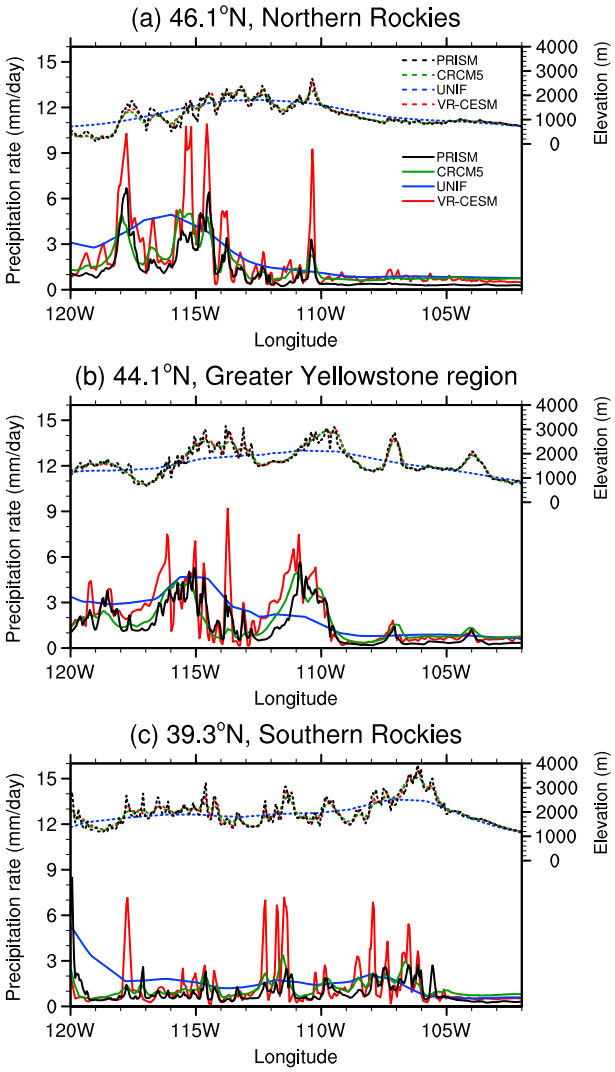

Figure 6. Variation of wintertime mean precipitation for VR-CESM, UNIF, CRCM5, and PRISM are shown in red, blue, green, and black, respectively, for three latitudes that transect the middle of the (a) Northern Rockies, (b) Greater Yellowstone region, and (c) Southern Rockies. The terrain heights are shown in dashed lines.

between mountains and plains, although the precipitation is slightly underestimated in the Northern Rockies and the Greater Yellowstone region and overestimated by 1–2 mm/d in the eastern part of the Southern Rockies. SCORR value between the VR-CESM simulation and observations is smaller for summer (0.66) than for winter (0.80) and for annual mean (0.75). Compared to VR-CESM, UNIF cannot reproduce the spatial variations of observed summertime precipitation in the mountains and tends to produce much more precipitation along the eastern flank of the mountains. Interestingly, the spatial distribution of precipitation simulated by CRCM5 is close to observations in most regions. One exception is that in Southern Rockies precipitation is overestimated by 0–1 mm/d in CRCM5. Note that along the eastern flank of the Rocky Mountains, the tongue-type band of precipitation simulated by UNIF is much more pronounced than in observations. Such bias is also present in VR-CESM but much weaker. This may indicate the overestimation of water vapor surge from the Gulf of Mexico. In autumn, the precipitation bias in VR-CESM is relatively smaller than in other seasons, and precipitation is overestimated in CRCM5 as in spring with smaller biases. Table 2 summarizes the range of SCORRs for each year from 1981 to 2005 and SCORR for the mean of 1981–2005. The difference of SCORRs is around 0.2 to 0.6 year by year in VR-CESM and CRCM5, corresponding to the large interannual variations of precipitation that can lead to large biases in certain years.

To further illustrate the modeled precipitation biases along the topography, the variations of wintertime mean precipitation with elevation at three latitudes (46.1°N, 44.1°N, and 39.3°N) are plotted in Figure 6. These three latitudes were chosen as they transect the middle of the three regions (Northern Rockies, Greater Yellowstone region, and Southern Rockies), respectively (Figure 2a). The variations of standard deviations are plotted in Figure S10, and they track closely with the variations of mean precipitation. Observed wintertime precipitation varies greatly with elevation, with relatively higher precipitation along the western (i.e., windward) side of mountain ridges. In contrast to UNIF that simulates a very smoothed precipitation curve over the mountain ridges and the valleys, VR-CESM is effective at capturing the variation of precipitation with elevation. However, the VR-CESM simulated precipitation peaks are too high compared to PRISM observations. For example, in the Northern Rockies the observed precipitation rate is 3–6 mm/d around 114–116°W (on the west side of the mountain ridges at 112–114°W), whereas the VR-CESM simulated precipitation rate peaks at about 10 mm/d (Figure 6a). In the Greater Yellowstone region, VR-CESM also simulates a higher precipitation rate from 113°W to 110°W along the windward side of the ridges (Figure 6b). Overestimation of precipitation peaks along the western flank of the mountain ranges is also found in the Southern Rockies in the VR-CESM simulation (Figure 6c). Compared to VR-CESM, CRCM5 simulates a smoother precipitation curve than VR-CESM, which makes the peak of CRCM5 match more closely to observations. However, the peaks of precipitation in CRCM5 are mostly smaller than observations especially in the Northern Rockies and Greater Yellowstone region. Note that as VR-CESM employs unsmoothed topography, it is reasonable to suspect that these precipitation peaks may be smoothed out and reduced to some extent with topographic smoothing employed. On the other hand, as found in VR-CESM, CRCM5 also tends to overestimate the precipitation in the windward of the mountain ranges and underestimate it in the leeward, although with less biases than VR-CESM. The smoothed curves of precipitation in UNIF also exhibit more precipitations in the windward side of the mountains than the observations. The windward precipitation biases in VR-CESM may be related to the model's deficiency in simulating winter storm activity and water vapor transport, as will be discussed in section 5. These biases

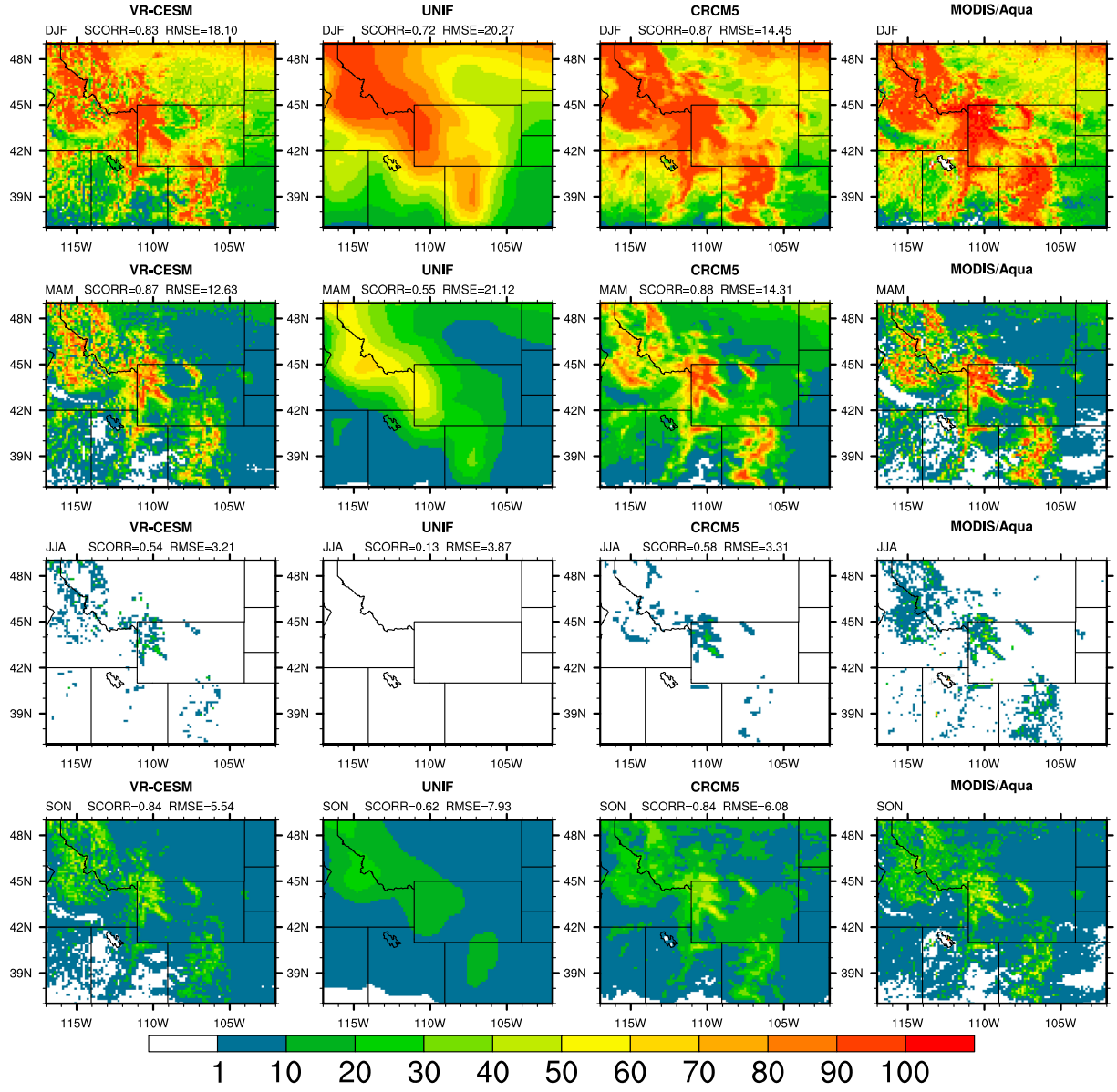

Figure 7. As in Figure 3 but for (top row) winter, (second row) spring, (third row) summer, and (fourth row) autumn mean snow cover fraction (SCF; %).

may also be related to the diagnostic precipitation scheme in CAM5 that is unable to transport orographically induced precipitation across the mountain ridgeline (Rhoades et al., 2016), which is expected to be improved with a prognostic microphysics scheme (Gettelman & Morrison, 2015).

4.1.3. Snowpack

Figure 7 shows the mean SCF in four seasons from the VR-CESM, UNIF, and CRCM5 simulations, compared with MODIS/Aqua observations. The difference of each simulation relative to observations is shown in Figure S11. The spatial patterns of MODIS/Terra SCF are very similar to those of MODIS/Aqua SCF except that MODIS/Terra SCF is slightly larger in mountainous regions. Observed mean SCF is mostly greater than 10% in the mountains in all the seasons except summer. Observed SCF is larger in winter than in other seasons, with the surface almost entirely covered by snow (i.e., with SCF around 100%) in the high mountains in winter. In spring, observed SCF is mostly above 80% in the mountain ridges. In summer, snow cover is still observed in high mountain ridges, although much less (mostly below 30%). Observed SCF in autumn is mostly below 60% in the mountains, which is smaller than in spring.

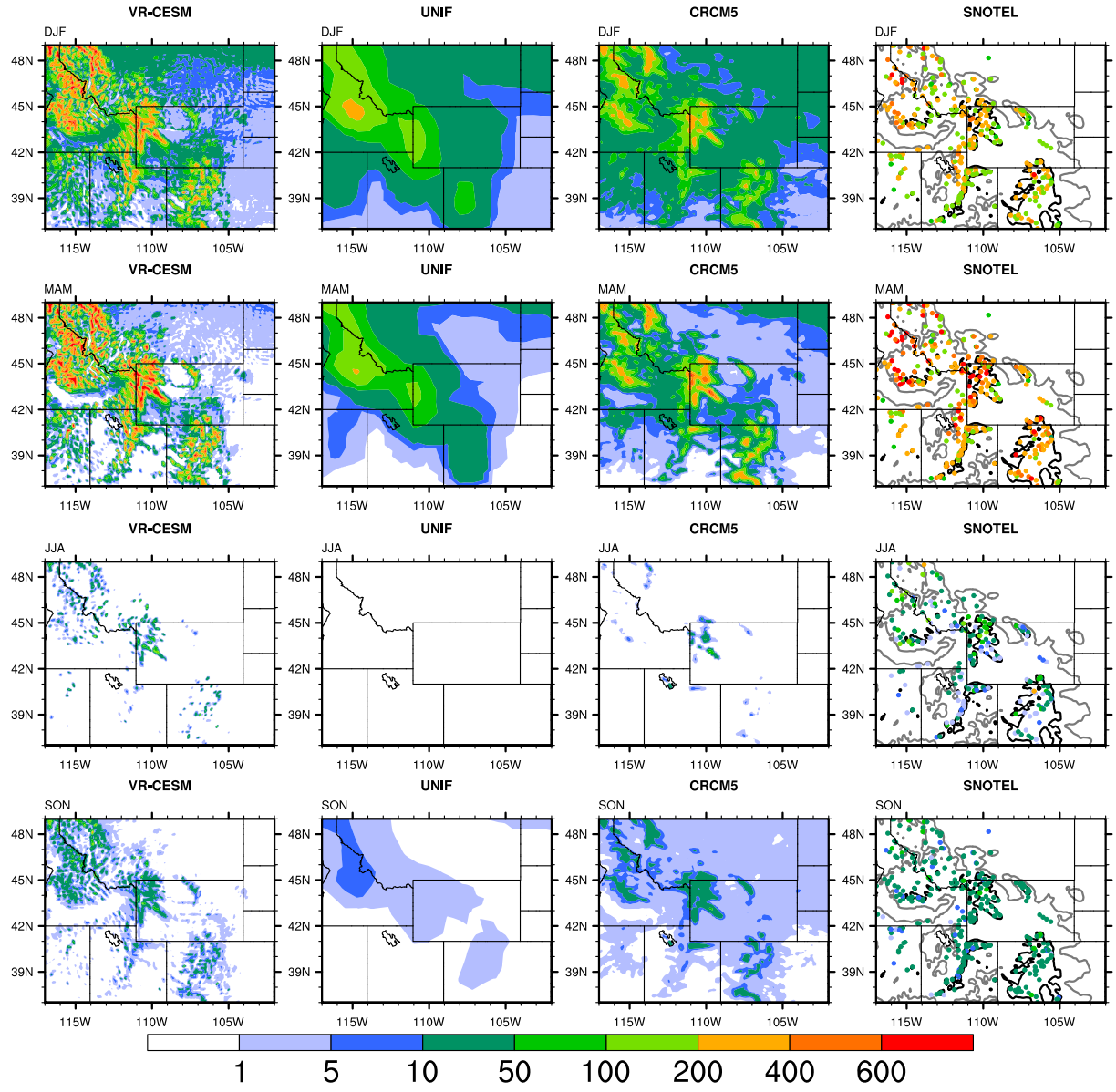

Figure 8. As in Figure 7 but for snow water equivalent (SWE; mm). (fourth column) The gray and black lines denote the elevations of 1,500 m and 2,500 m, respectively.

UNIF is able to simulate higher SCF in winter than in other seasons. However, it cannot resolve the observed spatial patterns of SCF. UNIF also cannot simulate the persistence of snow cover in summer. In contrast, VR-CESM and CRCM5 capture the observed spatial distribution of SCF, especially over the mountain ridges. VR-CESM and CRCM5 also capture the larger extent of snow cover in winter and the persistence of snow cover in summer. Although wintertime VR-CESM-simulated SCF matches closely with observations in the mountain ridges, it is lower than observed SCF (still above 90%) by 10%–40% in the regions around the mountain ridges and by 40–70% in some regions between the mountains ridges or in the eastern side of mountain ridges. In the plains to the east and the south of Rocky Mountains, VR-CESM also overestimates SCF by 5–30%, which can in part explain the overestimation of temperature in these regions (section 4.1.1). In spring, VR-CESM produces SCF biases within ±30% in the mountains with uniformly underestimated SCF by 10–40% in the Southern Rockies. Compared to VR-CESM, CRCM5 produces similar magnitude of SCF biases in the mountains but tends to overestimate SCF by 5–30% in larger regions of the plains. Given the overall accuracy of MODIS

observations is around 88%–93% (Hall & Riggs, 2007), these biases generally exceed the uncertainty in the MODIS observations. However, MODIS monthly SCF is obtained based on the available measurements in the swaths along the satellite orbits at specific time stamps (Hall et al., 2006). By comparison, modeled SCF at all model time steps is averaged to produce the seasonal mean SCF, which may smooth out the short-duration snow cover. Therefore, the difference in the sample strategy between model simulations and MODIS observations may partly explain the underestimation of SCF in VR-CESM at the edges of densely snow-covered areas (i.e., the mountains ridges).

Figure 8 compares snow water equivalent (SWE) from VR-CESM, UNIF, and CRCM5 simulations with SNOTEL observations (differences between simulation and observation are shown in Figure S12). These SNOTEL stations are in the mountain regions (elevations >900 m) with relatively larger SCF (Figure 7). The observations show that SWE is largest (mostly between 50 and 1,100 mm) in spring and second largest (mostly between 50 and 600 mm) in winter in the mountains. VR-CESM effectively captures the spatial variability of SWE in winter and spring. VR-CESM simulates comparable magnitudes of SWE with the observations with the biases mostly within ±200 mm, except at some stations in Southern Rockies where the biases are around −200 to −400 mm. CRCM5 also captures the observed spatial distributions of SWE but tends to simulate a smaller SWE with the biases mostly from −100 mm to −400 mm compared to SNOTEL observations. In summer, observed snowpack still exists with the mean SWE mostly below 100 mm in the mountains. UNIF simulates no snowpack in summer, whereas VR-CESM captures the persistence of snow (although with slightly lower SWE and coverage area). CRCM5 also capture the persistence of snow but with smaller SWE compared to VR-CESM and SNOTEL observations. As expected, with higher elevation topography resolved in VR-CESM, it is more likely that snowpack persists for a longer period in VR-CESM than in UNIF. In autumn, both VR-CESM and CRCM5 simulate comparable SWE (mostly around 10–50 mm) with observations. Note that smaller SWE in CRCM5 compared to VR-CESM and SNOTEL can in part be attributed to the larger surface air temperature (section 4.1.1) and smaller winter precipitation (section 4.1.2) as simulated in CRCM5.

4.2. Seasonal Evolution

Figure 9 shows the seasonal evolution of T_{mean}, T_{max}, and T_{min} averaged at SNOTEL stations in the Northern Rockies, Greater Yellowstone region, and the Southern Rockies from VR-CESM, UNIF, and CRCM5 simulations and SNOTEL observations. The standard deviations of T_{mean}, T_{max}, and T_{min} are also shown in the figure. In general, all the simulations capture the seasonal cycle of temperature in the mountains. Moreover, VR-CESM simulates lower temperatures by 1–6°C than UNIF in the Northern Rockies and Greater Yellowstone region, and by up to 6–9°C in the Southern Rockies. The difference of temperatures (for T_{mean}, T_{max}, and T_{min}) between VR-CESM and UNIF is smallest in the Northern Rockies and largest in the Southern Rockies. This corresponds to the smallest and largest elevation differences between VR-CESM and UNIF simulations in these two regions, respectively (Figure 2). Compared to observations, VR-CESM generally performs better than UNIF in simulating temperature (especially for T_{min}) in the warm season (May to September) but shows larger cold biases by up to −6°C in the cold season (December to April). Compared to VR-CESM, CRCM5 simulates constantly larger T_{mean} and T_{min} by 2–7°C in these three regions, making CRCM5 simulations more consistent with observations in the cold season but more deviated from observations in the warm season. For T_{max}, CRCM5 simulates smaller difference between winter and summer, which is closer to the observations than VR-CESM. Note that the standard deviations of temperatures are mostly below 3°C, and the aforementioned large biases (e.g., T_{min} cold bias in winter for VR-CESM and T_{min} warm bias in summer for CRCM5) exceed the standard deviations. Underestimation of temperature by VR-CESM in the cold season may be related to the model bias in simulating temperature inversions in the mountain-valley regions (section 4.1.1). It may also indicate the model deficiency in representing land surface processes such as surface albedo and vegetation treatment in CLM (Chen et al., 2014).

Figure 10 shows the seasonal evolution of precipitation as well as the precipitation accumulation during the water year averaged at the SNOTEL stations from VR-CESM, UNIF, and CRCM5 simulations and SNOTEL observations. Observed precipitation is larger from October to May than in other months. Standard deviations (interannual variations) of precipitation are larger (1–2 mm/d) during November to February than in other months, especially for the Northern Rockies (1.5–2 mm/d). In Northern Rockies, observed precipitation shows an annual cycle of precipitation with maximum from November through January and minimum from July through September. In the Greater Yellowstone and Southern Rockies, more precipitation is observed in

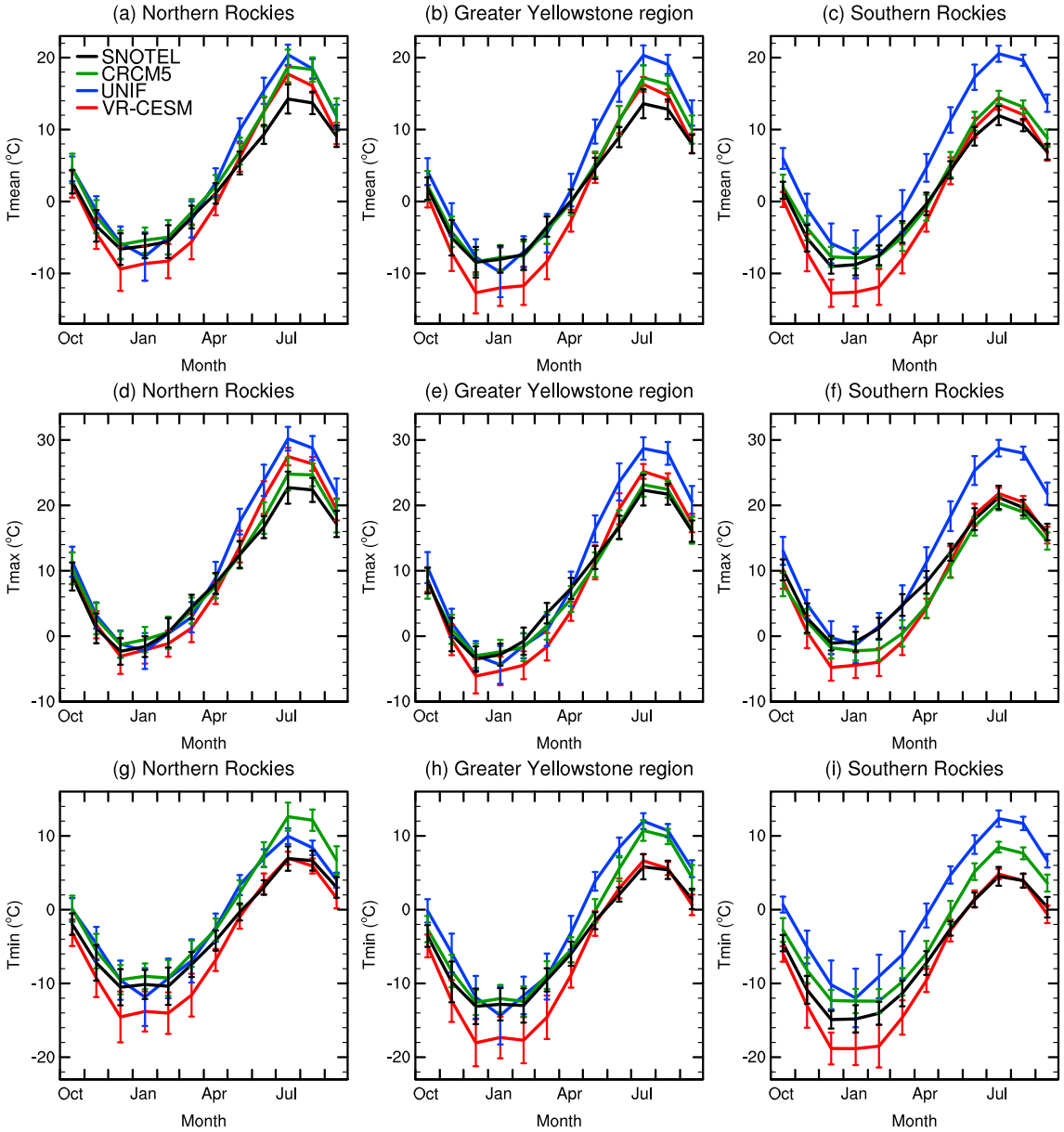

Figure 9. Evolution of monthly mean, mean daily maximum, and mean daily minimum temperature (T_{mean}, T_{max}, and T_{min}, respectively; °C) averaged at the 56, 61, and 50 SNOTEL stations in the Northern Rockies, Greater Yellowstone region, and Southern Rockies during the water year (1 October to 30 September). The vertical bars denote the standard deviations.

spring, which is comparable to the precipitation in late autumn and winter. This result agrees with that of Wang et al. (2009), who used multiple data sets to identify the seasonal variations of precipitation in the western United States.

Compared to the observations, both VR-CESM and UNIF capture the seasonal evolution of precipitation in the Northern Rockies, and CRCM5 simulates less variations of precipitation from November to May. VR-CESM overestimates the precipitation from December to March, while UNIF and CRCM5 underestimate it, which is consistent with the spatial distributions of wintertime precipitation (Figures 4 and 5). In the Greater Yellowstone region, all the simulations capture the seasonal evolution of precipitation, albeit with the overestimation and underestimation of precipitation from December to March found in VR-CESM and UNIF, respectively. In the Southern Rockies, UNIF is unable to capture the seasonal evolution of precipitation, while VR-CESM and CRCM5 are able to do it. Overestimation of winter precipitation in VR-CESM may be related to

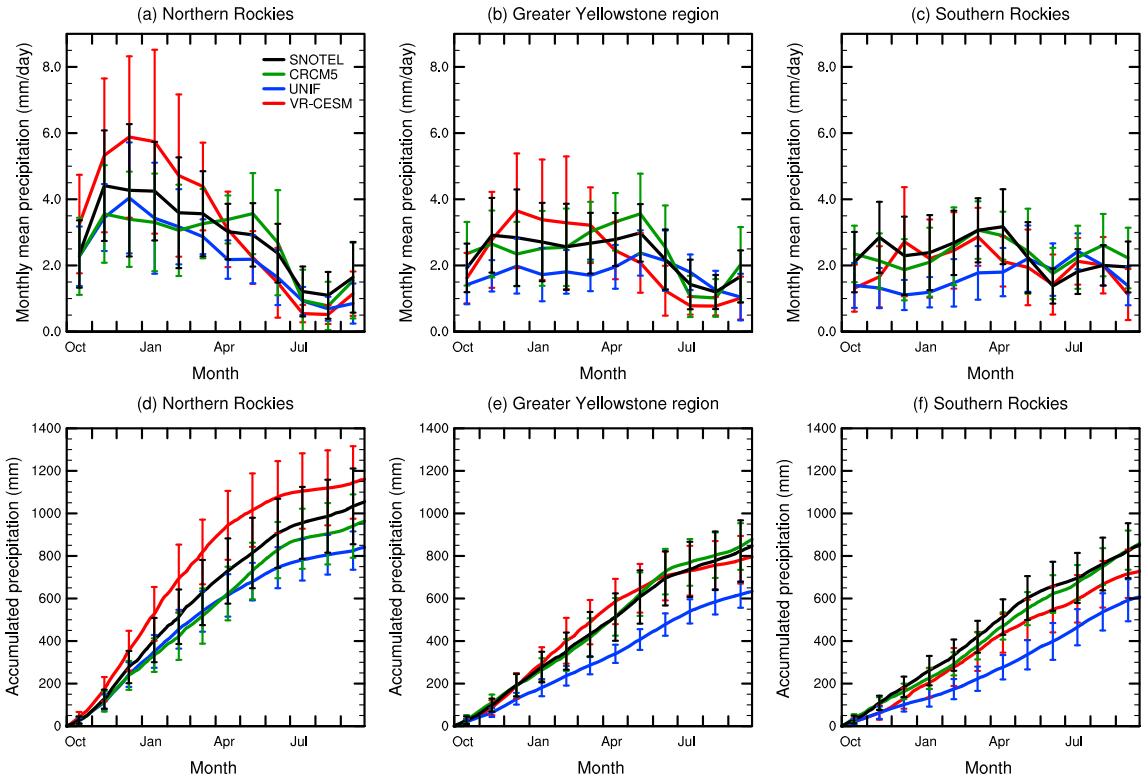

Figure 10. Evolution of (a–c) daily precipitation rate (given in monthly mean) and (d–f) accumulated precipitation averaged at the 70, 59, and 48 SNOTEL stations in the Northern Rockies, Greater Yellowstone region, and Southern Rockies during the water year. The vertical bars denote the standard deviations. Note that for Figures 10d–10f accumulated precipitation, only the standard deviations at the middle of each month are displayed.

stronger winter storm activities and stronger water vapor transport from the Pacific Ocean, as will be discussed in section 5. Note that both VR-CESM and UNIF simulations underestimate the precipitation in middle-late spring (April and May). A similar underestimation of precipitation is also found in previous model simulations (Wang et al., 2009), which showed that three of six RCMs they used cannot reproduce the late-spring precipitation in the Rocky Mountains. In this transitory season when polar cold air and subtropical warm air meet to form precipitation in the Rocky Mountains, it is reasonable to suspect that it is more difficult for climate models to correctly simulate the movement and collision of both cold air and warm air. However, in contrast to the underestimation of precipitation in VR-CESM and UNIF, CRCM5 overestimates precipitation in this season. In addition, VR-CESM also simulates smaller precipitation than the observations in summer in the Northern Rockies and Greater Yellowstone region. This may be due to smaller convective precipitation in summer simulated by VR-CESM than by UNIF, as the physical parameters, which are largely tuned for UNIF, are kept identical in VR-CESM, but only the time steps are reduced (Table 1). Williamson (2008) showed that with reduced physics time step, convection precipitation is decreased in an earlier version of CAM (CAM3), probably because the convection becomes less active and thus performs less vertical redistribution and condensation of water vapor with the shorter time steps.

Corresponding to the evolution of precipitation rate, VR-CESM simulates larger accumulated precipitation in all three regions than UNIF (Figures 10d–10f). Compared to the observations, VR-CESM overestimates the annual precipitation in the Northern Rockies but produces close total precipitation in the Greater Yellowstone region, although there is an offset of smaller precipitation in April–September by larger precipitation in November-to-March (Figure 10b). CRCM5 underestimates the annual precipitation by 100 mm in the Northern Rockies but simulates annual precipitation similar to observations in the Greater Yellowstone region. In the Southern Rockies, VR-CESM and CRCM5 simulate smaller accumulated precipitation than observations before April, but CRCM5 simulates larger precipitation from May to August. VR-CESM underestimates the total precipitation by 130 mm in this region.

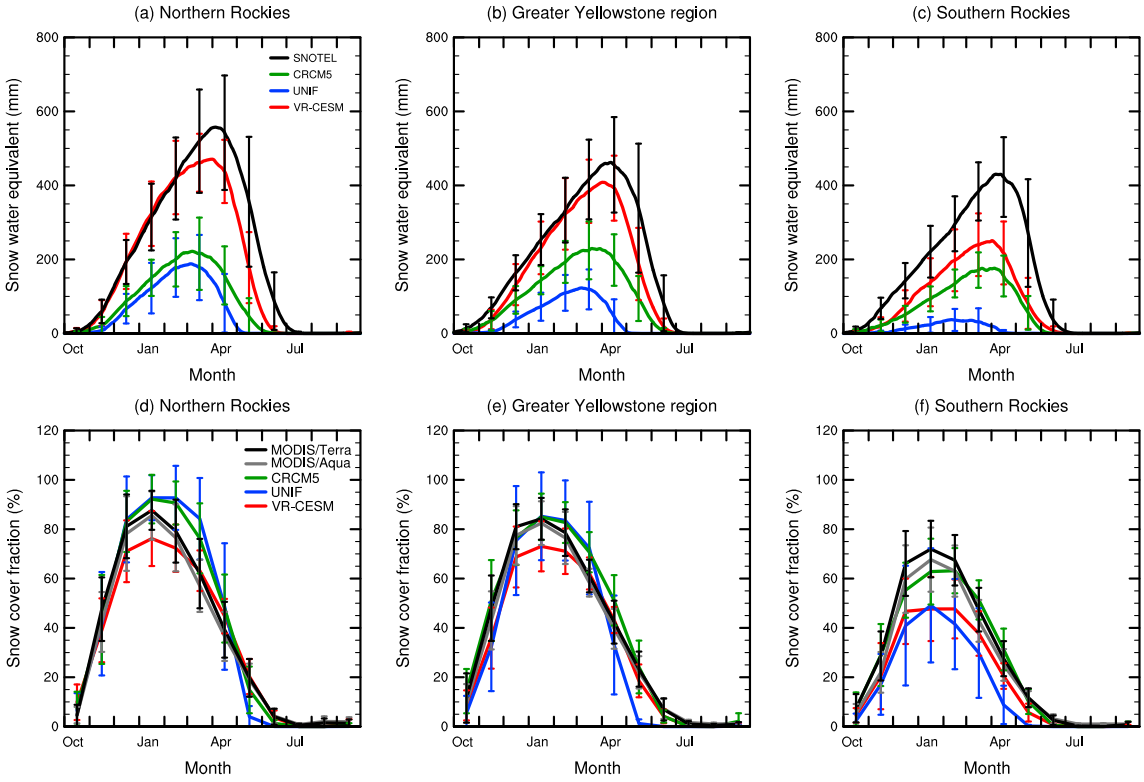

Figure 11. Evolution of (a–c) daily snow water equivalent (SWE; mm) and (d–f) monthly snow cover fraction (SCF; %) averaged in the Northern Rockies, Greater Yellowstone region, and Southern Rockies. Note that SWE is averaged at the SNOTEL stations as in Figure 10, while SCF is averaged for all the grids in the three regions shown in Figure 2. The vertical bars denote the standard deviations. For SWE (Figures 11a–11c), only the standard deviations at the middle of each month are displayed.

The seasonal evolution of regional mean SWE and SCF in the three regions is shown in Figure 11. For each region, SWE is averaged at the SNOTEL stations and SCF is calculated from the results at all the grids. The observed SWE distinctly shows the snow accumulation from October to April and the snowmelt later in all the three regions. The peaks of observed SWE occur in early-to-middle April, which corresponds to a period of T_{mean} around 0°C (Figures 9a–9c). Unlike SWE, observed SCF is larger throughout the winter and decreases in spring and summer. SCF peaks earlier than SWE mainly because SCF accounts for snow cover in both the mountains and surrounding regions while SWE is mainly contributed from the snow amount in the higher mountains (>900 m). Another reason is that snowpack becomes much patchier with increasing snow density in melting periods, leading to less snow cover areas than in snowfall periods given a similar snow depth (Niu & Yang, 2007).

Compared to SNOTEL observations, VR-CESM captures the temporal evolution of SWE but underestimates the magnitude of SWE peaks in all the three regions (especially in the Southern Rockies). UNIF and CRCM5 simulate much smaller SWE than the observations and tend to simulate the occurrence of SWE peaks 10 to 20 days earlier than the observations. UNIF and CRCM5 also simulate the shorter duration of snow cover, which is consistent with the results of simulated seasonal spatial distribution of SWE in section 4.1 (Figure 8). For SCF, VR-CESM also captures the seasonal evolution of observed SCF, although SCF remains underestimated in winter in all the three regions. In contrast, UNIF (CRCM5) produces 10–25% (5–15%) larger SCF in February and March than observations in the Northern Rockies and the Greater Yellowstone region. In the Southern Rockies, UNIF simulates similar SCF as VR-CESM from October to January but 5–10% smaller than VR-CESM from February to May, which deviates more from the observations, while CRCM5 shows only slightly smaller SCF than the observations. Overall, although model biases still exist, VR-CESM shows substantial improvements in the temporal evolution of SWE compared to UNIF and CRCM5, especially for the timing and magnitude of SWE peaks. VR-CESM simulates better temporal

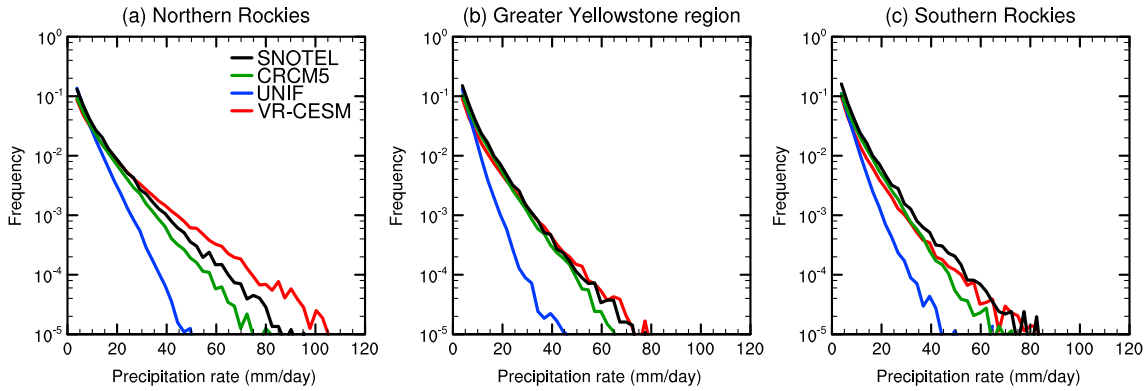

Figure 12. The frequency distributions of daily precipitation rate (mm/d) calculated at SNOTEL stations in the Northern Rockies, Greater Yellowstone region, and Southern Rockies. The minimum precipitation rate recorded by SNOTEL was 2.54 mm/d (i.e, 0.1 in/day) (section 3); thus, we only include the frequencies of simulated precipitation rate greater than 2.54 mm/d.

evolution of SCF than CRCM5 in the Northern Rockies and Greater Yellowstone but shows larger biases of SCF in the Southern Rockies.

Snowpack is closely associated with the surface temperature and precipitation. Thus, biases in temperature and precipitation may lead to biases in snowpack. In particular, the underestimation of SWE and SCF in the Southern Rockies by VR-CESM can be partly attributed to the smaller precipitation in VR-CESM in this region (Figures 10c and 10f). However, VR-CESM simulates larger precipitation and colder temperature in winter in the Northern Rockies and the Greater Yellowstone region but a smaller SWE compared to SNOTEL observations. As discussed in section 3, there is probably an undercatch of precipitation in the SNOTEL observations, which can in part explain the positive precipitation biases in VR. Note that the model underestimation of precipitation compared to SNOTEL observations in the late spring (April–May) (Figures 10a and 10b) may also contribute to the SWE and SCF underestimations in VR-CESM. In addition, the model biases in snowpack may be related to the discrepancy in the partition of precipitation into snowfall and rainfall (section 6) as well as in the snow physics for representing the snow accumulation and melt at the land surface (Chen et al., 2014).

4.3. Frequency Distribution of Daily Precipitation

Figure 12 shows the frequency distribution of daily precipitation calculated at the SNOTEL stations from the VR-CESM, UNIF, and CRCM5 simulations and SNOTEL observations in the three regions during 1981–2005. The frequencies of effective precipitation days (defined as daily precipitation $\geq$ 2.54 mm, which is the lower limit of nonzero precipitation recorded by SNOTEL) and heavy precipitation events (defined as daily precipitation $\geq$ 25 mm) are also given in Table 3. The observed frequency shows an exponential decay with increasing precipitation rate (Figure 12). In total, the observed frequency of effective precipitation days is similar (about 34%–35%) in the three regions (Table 3). For the heavy precipitation events, observed frequency is higher in the Northern Rockies (1.71%) than in the Greater Yellowstone region (0.82%) and in the Southern Rockies (0.92%).

Table 3
Frequencies (%) of Effective Precipitation Days (Daily Precipitation ≥ 2.54 mm) and Heavy Precipitation Events (Daily Precipitation ≥ 25 mm) From the Simulations and Observations in Three Regions

Region	VR-CESM	UNIF	CRCM5	SNOTEL
		Effective precipitation days		
Northern Rockies	26.0%	28.1%	25.8%	34.2%
Greater Yellowstone	21.6%	22.2%	26.0%	34.0%
Southern Rockies	21.1%	20.3%	25.8%	35.4%
		Heavy Precipitation Events		
Northern Rockies	***2.33%***	0.23%	***1.18%***	1.71%
Greater Yellowstone	***0.84%***	0.04%	***0.67%***	0.82%
Southern Rockies	0.57%	0.08%	0.60%	0.92%

Note. Effective precipitation days are defined according to the lower limit of SNOTEL observations. Simulation results that are not statistically different from the observations at the 0.1 level are given in bold italic.

Compared to the observations, all the simulations produce exponential decays in frequency with the precipitation rate. However, UNIF simulates a much faster decay in all the three regions. Significant underestimation of frequencies, especially for heavy precipitation events, is found in UNIF in all three regions. In contrast, VR-CESM and CRCM5 show a similar decay rate as the observations. VR-CESM simulates higher frequencies of heavy precipitation events in the Northern Rockies than observations. However, there is observational evidence that during heavy precipitation events when winds are strong, large undercatches of precipitation can occur (Rasmussen et al., 2012). Therefore, the

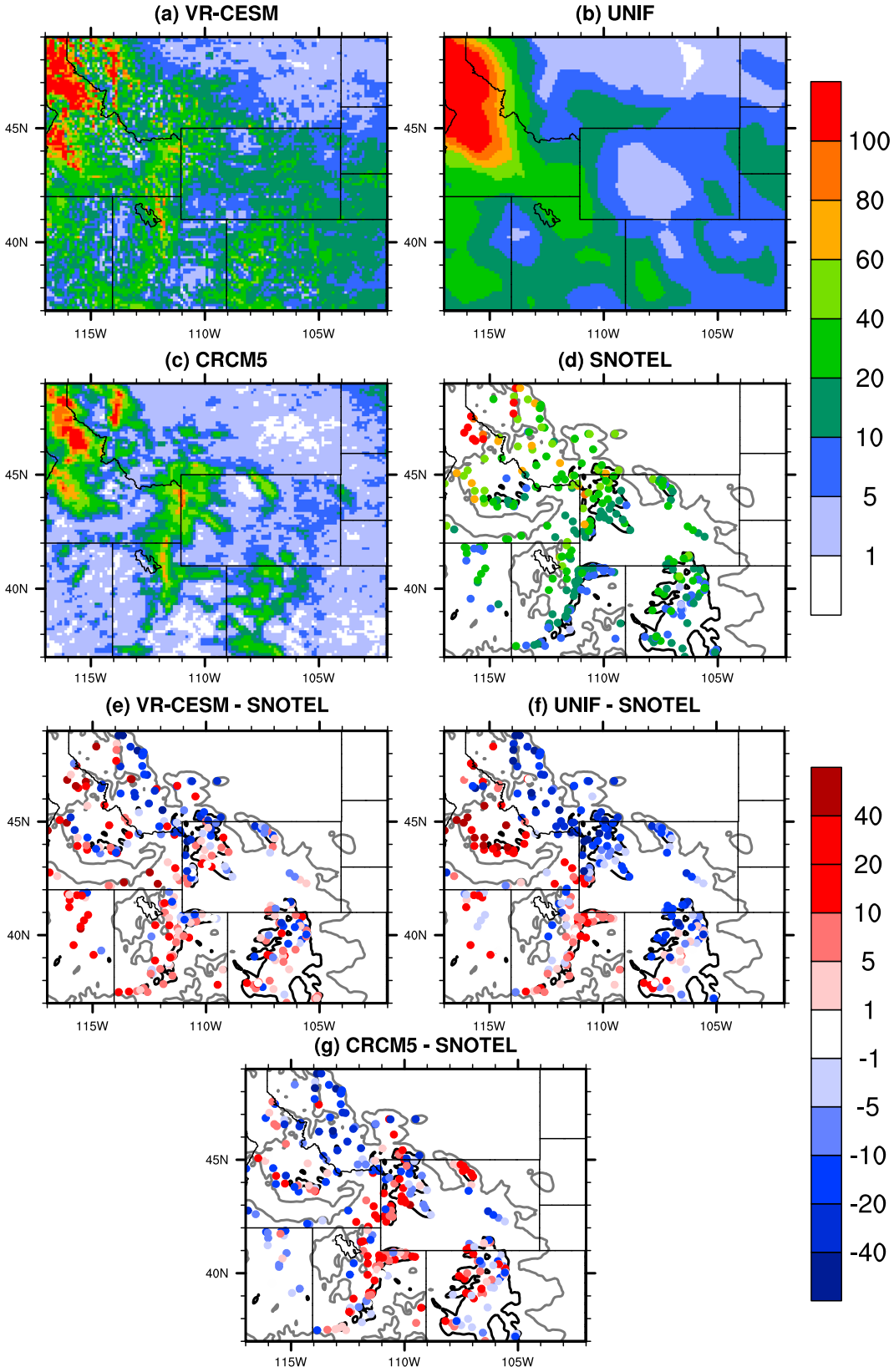

Figure 13. (a–d) Total number of rain-on-snow (ROS) days during 1986–2005 from VR-CESM, UNIF, and CRCM5 simulations, and SNOTEL observations. (e–g) Differences between each simulation and SNOTEL observations at the SNOTEL stations. The gray and black lines in Figures 13d–13g denote the elevations of 1,500 m and 2,500 m, respectively.

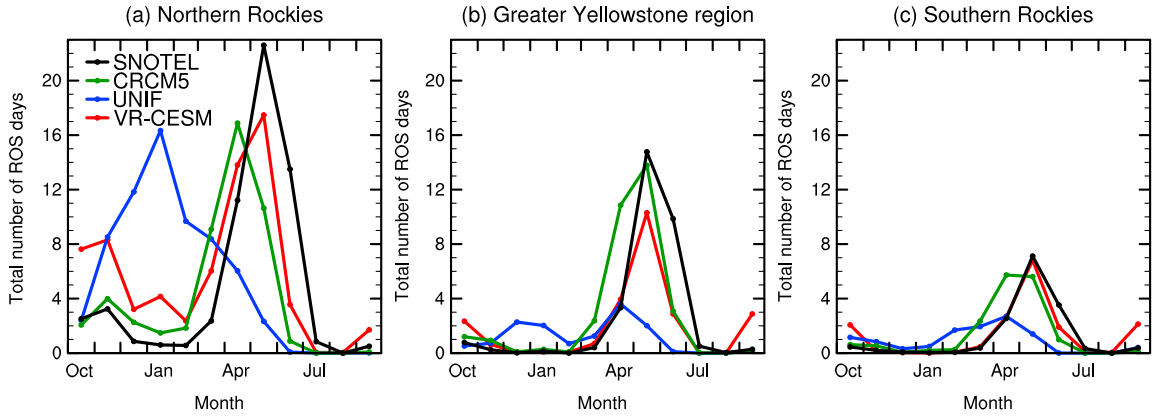

Figure 14. Monthly cumulative number of ROS days during 1986–2005 averaged at SNOTEL stations in the (a) Northern Rockies, (b) Greater Yellowstone region, and (c) Southern Rockies.

overestimation of frequencies of heavy precipitation may be not the case or at least not so strong. VR-CESM underestimates frequencies for a broad range of precipitation rates in the Southern Rockies. CRCM5 distinctly underestimates the frequencies of heavy precipitation in all the three regions. Note that the model biases in the heavy precipitation are generally consistent with the biases in total precipitation. This can be expected since the frequencies of small-to-medium precipitation (daily precipitation $<$ 25 mm) in the simulations are very close to the observations. Overall, the frequency of heavy precipitation events simulated by VR-CESM is very close to the observation in the Greater Yellowstone region and is comparable to the observations in the Northern Rockies and Southern Rockies (Table 3). In contrast, the frequency of heavy precipitation events simulated by UNIF is about 1 order of magnitude lower than that by VR-CESM (Table 3). For effective precipitation days, VR-CESM and UNIF simulate similar frequencies, which are both lower than observations, and CRCM5 simulates 3–5% larger frequencies that are closer to observations (Table 3).

4.4. ROS Days

Figure 13 shows the comparison of the total number of ROS days during 1986–2005 from the VR-CESM, UNIF, and CRCM5 simulations and SNOTEL observations. Observed ROS events occur most frequently in the Northern Rockies, with more than 20 ROS days at most SNOTEL stations in this region and more than 100 ROS days at some stations in the northern part of this region. In the Greater Yellowstone region, observations indicate that the number of ROS days is between 10 and 60 at most stations, with four stations having greater than 60 ROS days. In the Southern Rockies, ROS events occur least frequently with 5–60 ROS days at most stations. Compared to observations, all the simulations capture the geographic difference in the number of ROS days among the three regions. VR-CESM and CRCM5 reasonably reproduce the spatial distribution of the number of ROS days, while UNIF only simulates the general spatial distribution (specifically, it lacks the spatial heterogeneity seen in VR-CESM and CRCM5). UNIF simulates a smaller number of ROS days except in the western portions of the Northern Rockies. This is expected as both the spatial distribution of precipitation and SWE are better simulated by VR-CESM and CRCM5 than by UNIF. In the Greater Yellowstone region, CRCM5 simulates 5–20 more ROS events than VR-CESM, which is mainly due to larger number of ROS events in April and May (Figure 14b) induced by stronger precipitation (Figure 10b) in CRCM5.

The seasonal evolution of the number of ROS days averaged at SNOTEL stations in the Northern Rockies, Greater Yellowstone region, and the Southern Rockies is shown in Figure 14. In all of the three regions, observed ROS events mainly occur from April through June, peaking in May with 23, 15, and 7 ROS days in the three regions, respectively. ROS events occasionally occurred in other months. Compared to the observations, VR-CESM captures the seasonal evolution of the number of ROS days in all three regions, although the number of ROS days simulated by VR-CESM is smaller in May and June in both the Northern Rockies and the Greater Yellowstone region and is larger from October to March in the Northern Rockies. The biases of ROS occurrences in VR-CESM are closely related to the biases in precipitation as simulated by VR-CESM (Figures 10a–10c). In contrast, UNIF cannot capture the seasonal evolution of the number of ROS days in

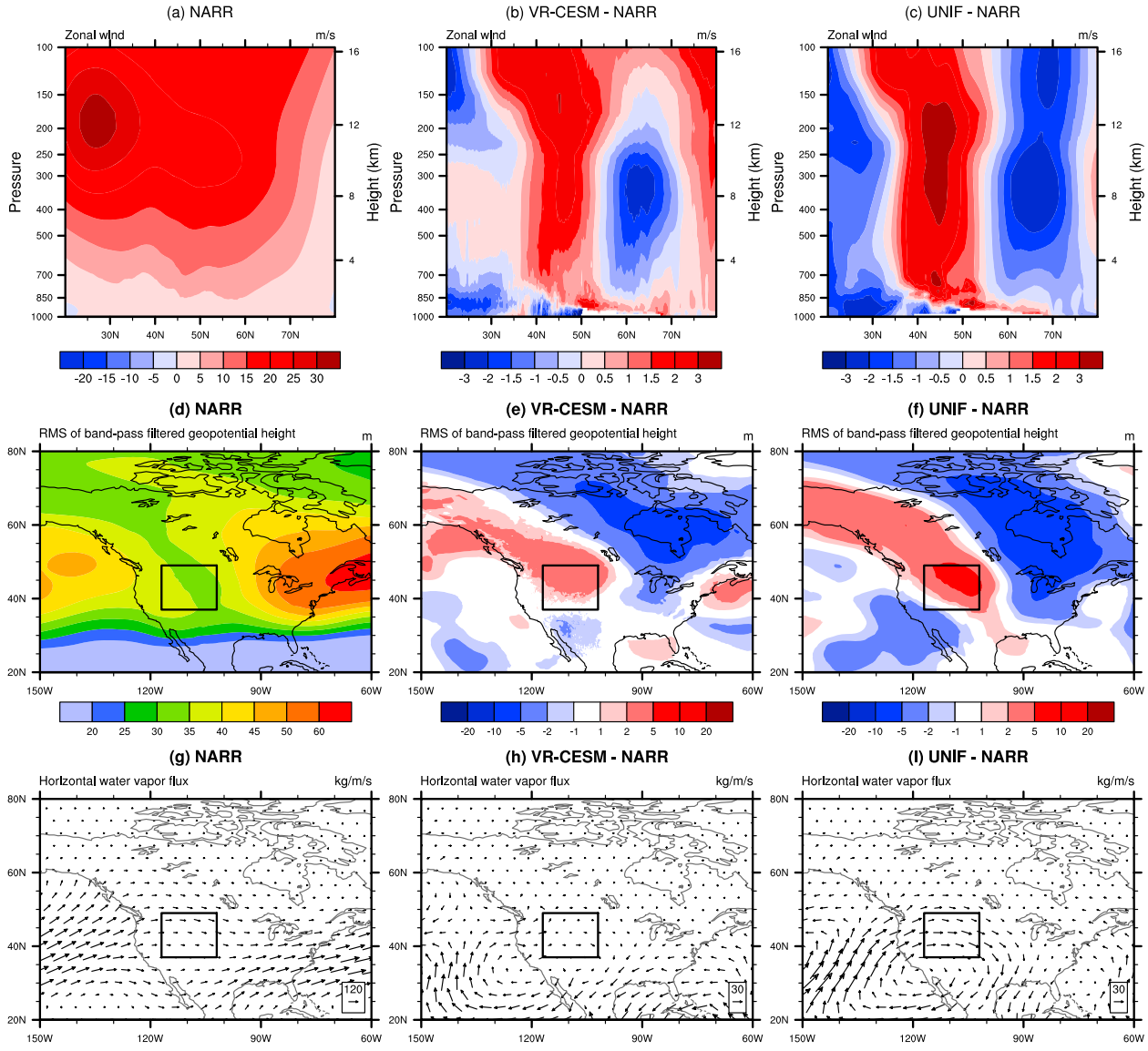

Figure 15. (a–c) Wintertime zonal winds (m s^{-1}) averaged at 102–125°W, (d–f) root-mean-square (RMS; m) of band-pass filtered 500 hPa geopotential height (at periods of 2.5–6 days), and (g–i) vertically integrated horizontal water vapor fluxes (kg m^{-1} s^{-1}) from NARR and the difference of VR-CESM and UNIF simulations relative to NARR. RMS of band-pass filtered 500 hPa geopotential height is a good indicator of storm activity (Blackmon, 1976), and here it is calculated from 6-hourly 500 hPa geopotential height (section 3). The black rectangle in Figures 15d–15i denotes the Rocky Mountain region. Note that zonal winds are averaged for a range of longitudes, which correspond to the east-western boundary of western U.S. including the Rocky Mountains and upwind regions (Figure 2).

all three regions. ROS events in UNIF occur more frequently in winter and early spring than the observations. Although CRCM5 can also capture the seasonal evolution of the number of ROS days, it tends to simulate more frequent occurrences of ROS events in March and April. This may be related to its overestimation of precipitation in April (in Northern Rockies and Greater Yellowstone; Figures 10a and 10b) and earlier snowmelt onset (Figure 11).

5. Discrepancies in the Large-Scale Meteorology

In this section, we investigate the large-scale meteorological conditions that are critical to understanding simulated wintertime precipitation in the Rocky Mountains.

First, we note that the jet stream is primarily responsible for the winter storm activity, which determines the precipitation in the Rocky Mountain region. Figures 15a–15c show the vertical cross section of winter zonal winds averaged from 102°W to 125°E from NARR and differences of VR-CESM and UNIF simulations relative to NARR. In general, both VR-CESM and UNIF simulate a similar position of the jet stream but with a weaker polar jet stream north of 55°N. This suggests a shift to a more meridional wind pattern in winter, which can enhance the broader meanders that are likely to form more winter storms. As shown in Figures 15d–15f, VR-CESM and UNIF simulate larger RMS of band-pass filtered 500 hPa geopotential height (at periods of 2.5–6 days) in the Rocky Mountain region and western Canada compared to NARR. This indicates more winter storm activity in these regions in the simulations than in NARR. On the other hand, at 35–55°N, VR-CESM and UNIF simulate stronger zonal winds by up to 3 m s^{-1}, which favors water vapor transport from the Pacific (Figures 15g–15i). VR-CESM (UNIF) simulates a 5–25 (15–40) kg m^{-1} s^{-1} larger water vapor flux into the western boundary of Rocky Mountain region compared to NARR (Figures 15g–15i). The enhance of wind storm activity and water vapor transport may lead to the overestimated precipitation in the Rocky Mountains, especially in the Northern Rockies and Greater Yellowstone region in VR-CESM (Figures 10a and 10b). Note that UNIF does not simulate larger precipitation as VR-CESM, which is mainly related to less locking of water vapor by the mountains to form precipitation due to the very smoothed topography used in UNIF (Figures 2 and 6).

Second, the tropospheric temperatures are also important for snow formation and snowfall. Both VR-CESM and UNIF simulate cold temperature bias by 1–3°C in the lower troposphere over the Rocky Mountain region (Figure S13). Generally, colder temperature tends to enhance the snow formation. This cannot explain the underestimation of SWE (Figures 11a–11c) in the mountains especially when the winter precipitation is overestimated in VR-CESM (Figure 10).

6. Conclusions

In this study, VR-CESM with a high resolution (0.125°) regionally refined grid is used to simulate the regional climate of the Rocky Mountain region of the United States. VR-CESM is compared with observations, as well as a coarse-resolution (quasi-uniform 1°) UNIF simulation and a regional climate simulation with CRCM5 at 0.11° resolution. In general, VR-CESM and CRCM5 capture the spatial patterns of temperature, precipitation, and snowpack in the Rocky Mountain region. In particular, VR-CESM and CRCM5 resolve the fine-scale features of these regional climate patterns associated with complex terrains. In contrast, UNIF is unable to do so due to the coarse resolution of orographic forcing in the model.

VR-CESM and CRCM5 also capture the seasonal evolution of temperature, precipitation, and snowpack, whereas UNIF simulates significantly reduced precipitation and SWE compared with VR-CESM and CRCM5 simulations and observations. However, although biases are found in both VR-CESM and CRCM5, they are significantly different in character. T_{min} biases are in similar magnitude (4–6°C) in the mountains for both VR-CESM and CRCM5, but there are cold biases of winter T_{min} for VR-CESM and warm biases of summer T_{min} for CRCM5. Winter precipitation is positively biased by VR-CESM in the Northern Rockies and the Greater Yellowstone region, while it is negatively biased in CRCM5. Despite winter precipitation overestimations in the western flanks of mountains in both VR-CESM and CRCM5, the overestimation in CRCM5 is not as strong as in VR-CESM. In the middle-to-late spring, VR-CESM tends to underestimate precipitation, while CRCM5 overestimates precipitation in the Northern Rockies and the Greater Yellowstone region. For snowpack, VR-CESM reproduces the seasonal evolution of SWE and SCF with the timing of SWE peak (around early-middle April) and duration of snow cover closely tracking with the observations. VR-CESM-simulated SWE is slightly smaller than observations in the Northern Rockies and Greater Yellowstone region and only 60% as much as observations in the Southern Rockies. In contrast, CRCM5 simulates only 40%–50% of observed SWE, with a 10–20 day earlier peak timing of SWE and a shorter duration of snowpack.

VR-CESM can also simulate the occurrence of heavy precipitation events with the frequencies in the same order of magnitude as the observations. The frequency of heavy precipitation events simulated by VR-CESM is close to observations in the Greater Yellowstone region (0.84% versus 0.82%) and is in the same magnitude with the observations in the Northern Rockies (2.33% versus 1.71%) and the Greater Yellowstone region (0.57% versus 0.92%). In contrast, UNIF simulates 1 order of magnitude lower frequencies for heavy precipitation events than the observations. In addition, VR-CESM can reproduce the spatial distribution

and seasonal evolution of the number of ROS days, while UNIF is unable to do so. CRCM5 can capture the spatial distribution of ROS events but simulates more occurrences of ROS events in March and April.

Overall, these results indicate that VR-CESM is effective in simulating the seasonal evolution of snowpack and precipitation as well as the heavy precipitation and ROS events. VR-CESM also shows comparable, and similarly reasonable, performance when compared with CRCM5, despite differences in the character of biases in VR-CESM. In some respects, VR-CESM performs better than CRCM5. In particular, VR-CESM simulates much better seasonal evolution and magnitude of SWE than CRCM5 (Figures 11a–11c). Nonetheless, as our purpose is to evaluate VR-CESM and help future model development, some biases in VR-CESM are noted. First, there are positive biases of winter precipitation in the Northern Rockies and Greater Yellowstone region, which is partly attributed to stronger winter storm activity induced by weaker polar jet stream and stronger water vapor transport from the Pacific Ocean in the model. Second, although VR-CESM simulates well the T_{min} in the warm season, it systematically underestimates T_{min} with negative biases of 4–6°C in the cold season. These biases can be partly explained by the model's inability to represent the synoptic-scale processes (e.g., downslope flow and accumulation of cold air) for temperature inversions in the valleys around the mountains (Lareau et al., 2013). These biases may also be reduced by further improving land surface processes, such as surface energy budget and treatment of underlying vegetation (e.g., Chen et al., 2014; Huang et al., 2016). Third, VR-CESM simulates considerably less SWE and SCF than observations in the Southern Rockies, which distinguishes this region from the relatively well-simulated Northern Rockies and Greater Yellowstone region. This can be partly explained by less precipitation simulated by VR-CESM in this region (Figure 10f).

Inconsistencies between VR-CESM modeled temperature, precipitation, and SWE are also found in the comparison with observations. For example, the model underestimation of temperature and overestimation of precipitation in winter in the Northern Rockies and Greater Yellowstone region are not consistent with the model underestimation of SWE in these two regions. This inconsistency can be partly explained by the undercatch of the precipitation in the SNOTEL observations. Additional sources of this inconsistency could be related to the representation of model physics in partitioning snowfall and rainfall. It has been shown that the ratio of snowfall to total precipitations can be quite different in different simulations (Figure S14). More model studies into snow formation and falling processes, and further observations of simultaneous snowfall and rainfall are vital to reduce the uncertainty in precipitation partitioning. As both temperature and precipitation may vary day by day, further investigation into the specific days when temperature is under a certain threshold (e.g., 0°C) and associated precipitation partitioning into snowfall and rainfall may better identify the reasons of the biases in snowpack. In addition, the model treatment of surface albedo and vegetation at the surface covered by snow can be largely biased, which can partly explain the SWE bias (Chen et al., 2014).

It should be noted that model physics parameterizations and associated parameters are not modified for the VR-CESM simulation from their default values, which are largely tuned for 1° resolution. This may hinder the improvement of model simulations when some scale-sensitive processes become more resolved. For example, the underestimation of precipitation in the late spring is present in both UNIF and VR-CESM simulations (Figure 10), which was also found in three of six RCMs (Wang et al., 2009). Such model biases may be reduced by using scale-aware parameterizations (e.g., Xie & Zhang, 2015). Despite this, our results show that the current version of VR-CESM has the capability to simulate the key aspects of regional climate in the Rocky Mountain region. Thus, it is a useful tool for understanding the processes that have shaped the past climate and will shape the future climate in this region.

Acknowledgments

This research is supported by University of Wyoming Tier-1 Engineering Initiative (High-Performance Computational Science and Engineering Cluster) funded by the State of Wyoming. Z. Lin was jointly supported by the Special Scientific Research Fund of the Meteorological Public Welfare Profession of China (grant GYHY01406021), National Key Research and Development Program of China (grant 2016YFC0402702), and the National Natural Science Foundation of China (grant 41575095). Support for A. M. Rhoades and P. A. Ullrich is provided by the U.S. DOE Office of Science projects "Multiscale Methods for Accurate, Efficient, and Scale-Aware Models of the Earth System" (contract DE-AC02-05CH11231) and "An integrated Evaluation of the Simulated Hydroclimate System of the Continental U.S." (contract DE-SC0016605). C. M. Zarzycki was supported by the Advanced Study Program at the NCAR. NCAR is sponsored by the National Science Foundation (NSF). We thank Katja Winger from the Université du Québec à Montréal (UQAM) in Canada for providing the Canadian Regional Climate Model version 5 (CRCM5) simulation results submitted to North American Coordinated Regional Climate Downscaling Experiment (NA-CORDEX) program. We thank the National Water and Climate Center (NRCS) of U.S. Department of Agriculture for maintaining the SNOTEL network and making the observation data set available to use (http://www.wcc.nrcs.usda.gov/snow/). We also thank the PRISM climate group in Oregon State University for providing the PRISM data set (http://prism.oregonstate.edu/) and appreciate Matt Doggett from the group for helpful discussions. We acknowledge the National Snow and Ice Data Center (NSIDC) for making MODIS snow cover data set available (http://nsidc.org/data/). NARR data are freely accessible online (https://rda.ucar.edu/datasets/ds608.0/). The 3-D interpolation package Dsgrid is available at http://www.ncarg.ucar.edu//ngmath/dsgrid/dshome.html. We would like to acknowledge the use of computational resources for conducting the model simulations (ark:/85065/d7wd3xhc) at the NCAR-Wyoming Supercomputing Center provided by the NSF and the State of Wyoming and supported by NCAR's Computational and Information Systems Laboratory. The CESM and VR-CESM simulation results can be obtained by contacting the corresponding author X. Liu (xliu6@uwyo.edu).

References

Berghuijs, W. R., Woods, R. A., Hutton, C. J., & Sivapalan, M. (2016). Dominant flood generating mechanisms across the United States. *Geophysical Research Letters*, *43*, 4382–4390. https://doi.org/10.1002/2016GL068070

Blackmon, M. L. (1976). A climatological spectral study of the 500 mb geopotential height of the northern hemisphere. *Journal of the Atmospheric Sciences*, *33*(8), 1607–1623. https://doi.org/10.1175/1520-0469(1976)033%3C1607:acssot%3E2.0.co;2

Chen, F., Liu, C., Dudhia, J., & Chen, M. (2014). A sensitivity study of high-resolution regional climate simulations to three land surface models over the western United States. *Journal of Geophysical Research: Atmospheres*, *119*, 7271–7291. https://doi.org/10.1002/2014JD021827

Christensen, J. H., Krishna Kumar, K., Aldrian, E., An, S.-I., Cavalcanti, I. F. A., de Castro, M., … Zhou, T. (2013). Climate Phenomena and their Relevance for Future Regional Climate Change. In T. F. Stocker, et al. (Eds.), *Climate Change 2013: The Physical Science Basis. Contribution of Working Group I to the Fifth Assessment Report of the Intergovernmental Panel on Climate Change* (pp. 1217–1308). Cambridge, UK: Cambridge University Press. https://doi.org/10.1017/CBO9781107415324.028

Daly, C., Halbleib, M., Smith, J. I., Gibson, W. P., Doggett, M. K., Taylor, G. H., … Pasteris, P. P. (2008). Physiographically sensitive mapping of climatological temperature and precipitation across the conterminous United States. *International Journal of Climatology*, *28*(15), 2031–2064. https://doi.org/10.1002/joc.1688

Dee, D. P., Uppala, S. M., Simmons, A. J., Berrisford, P., Poli, P., Kobayashi, S., … Vitart, F. (2011). The ERA-interim reanalysis: Configuration and performance of the data assimilation system. *Quarterly Journal of the Royal Meteorological Society*, *137*(656), 553–597. https://doi.org/10.1002/qj.828

Dennis, J. M., Edwards, J., Evans, K. J., Guba, O., Lauritzen, P. H., Mirin, A. A., … Worley, P. H. (2012). CAM-SE: A scalable spectral element dynamical core for the Community Atmosphere Model. *The International Journal of High Performance Computing Applications*, *26*(1), 74–89. https://doi.org/10.1177/1094342011428142

Déqué, M., & Piedelievre, J. P. (1995). High resolution climate simulation over Europe. *Climate Dynamics*, *11*(6), 321–339. https://doi.org/10.1007/bf00215735

Flanner, M. G., Zender, C. S., Randerson, J. T., & Rasch, P. J. (2007). Present-day climate forcing and response from black carbon in snow. *Journal of Geophysical Research: Atmospheres*, *112*, D11202. https://doi.org/10.1029/2006JD008003

Flato, G., Marotzke, J., Abiodun, B., Braconnot, P., Chou, S. C., Collins, W., … Midgley, P. M. (2013). Evaluation of climate models. In T. F. Stocker, et al. (Eds.), *Climate Change 2013: The Physical Science Basis. Contribution of Working Group I to the Fifth Assessment Report of the Intergovernmental Panel on Climate Change* (pp. 741–866). Cambridge, UK: Cambridge University. https://doi.org/10.1017/CBO9781107415324.020

Fox-Rabinovitz, M., Côté, J., Dugas, B., Déqué, M., & McGregor, J. L. (2006). Variable resolution general circulation models: Stretched-grid model intercomparison project (SGMIP). *Journal of Geophysical Research*, *111*, D16104. https://doi.org/10.1029/2005JD006520

Fox-Rabinovitz, M. S., Stenchikov, G. L., Suarez, M. J., & Takacs, L. L. (1997). A finite-difference GCM dynamical core with a variable-resolution stretched grid. *Monthly Weather Review*, *125*(11), 2943–2968. https://doi.org/10.1175/1520-0493(1997)125%3C2943:afdgdc%3E2.0.co;2

Gates, W. L. (1992). AMIP: The Atmospheric Model Intercomparison Project. *Bulletin of the American Meteorological Society*, *73*(12), 1962–1970. https://doi.org/10.1175/1520-0477(1992)073%3C1962:atamip%3E2.0.co;2

Gettelman, A., & Morrison, H. (2015). Advanced two-moment bulk microphysics for global models. Part I: Off-line tests and comparison with other schemes. *Journal of Climate*, *28*(3), 1268–1287. https://doi.org/10.1175/JCLI-D-14-00102.1

Giorgi, F., Jones, C., & Asrar, G. R. (2009). Addressing climate information needs at the regional level: The CORDEX framework. *World Meteorological Organization (WMO) Bulletins*, *58*(3), 175–183.

Groisman, P. Y., & Easterling, D. R. (1994). Variability and trends of total precipitation and snowfall over the United States and Canada. *Journal of Climate*, *7*(1), 184–205. https://doi.org/10.1175/1520-0442(1994)007%3C0184:vatotp%3E2.0.co;2

Guan, B., Waliser, D. E., Ralph, F. M., Fetzer, E. J., & Neiman, P. J. (2016). Hydrometeorological characteristics of rain-on-snow events associated with atmospheric rivers. *Geophysical Research Letters*, *43*, 2964–2973. https://doi.org/10.1002/2016GL067978

Guba, O., Taylor, M. A., Ullrich, P. A., Overfelt, J. R., & Levy, M. N. (2014). The spectral element method (SEM) on variable-resolution grids: Evaluating grid sensitivity and resolution-aware numerical viscosity. *Geoscientific Model Development*, *7*(6), 2803–2816. https://doi.org/10.5194/gmd-7-2803-2014

Haarsma, R. J., Roberts, M. J., Vidale, P. L., Senior, C. A., Bellucci, A., Bao, Q., … von Storch, J.-S. (2016). High Resolution Model Intercomparison Project (HighResMIP v1.0) for CMIP6. *Geoscientific Model Development*, *9*(11), 4185–4208. https://doi.org/10.5194/gmd-9-4185-2016

Hall, D. K., & Riggs, G. A. (2007). Accuracy assessment of the MODIS snow products. *Hydrological Processes*, *21*(12), 1534–1547. https://doi.org/10.1002/hyp.6715

Hall, D. K., Riggs, G. A., & Salomonson, V. V. (2006). MODIS snow and sea ice products. In J. J. Qu, et al. (Eds.), *Earth Science Satellite Remote Sensing: Vol. 1: Science and Instruments* (pp. 154–181). Berlin: Springer. https://doi.org/10.1007/978-3-540-37293-6_9

Harris, L. M., & Lin, S.-J. (2013). A two-way nested global-regional dynamical Core on the cubed-sphere grid. *Monthly Weather Review*, *141*(1), 283–306. https://doi.org/10.1175/mwr-d-11-00201.1

Harris, L. M., & Lin, S.-J. (2014). Global-to-regional nested grid climate simulations in the GFDL high resolution atmospheric model. *Journal of Climate*, *27*(13), 4890–4910. https://doi.org/10.1175/jcli-d-13-00596.1

Hsu, C.-P. F., & Wallace, J. M. (1976). The global distribution of the annual and semiannual cycles in precipitation. *Monthly Weather Review*, *104*(9), 1093–1101. https://doi.org/10.1175/1520-0493(1976)104%3C1093:tgdota%3E2.0.co;2

Huang, X., Rhoades, A. M., Ullrich, P. A., & Zarzycki, C. M. (2016). An evaluation of the variable-resolution CESM for modeling California's climate. *Journal of Advances in Modeling Earth Systems*, *8*(1), 345–369. https://doi.org/10.1002/2015MS000559

Huang, X., & Ullrich, P. A. (2017). The changing character of twenty-first century precipitation over the western United States in the variable-resolution CESM. *Journal of Climate*, *30*(18), 7555–7575. https://doi.org/10.1175/JCLI-D-16-0673.1.

Hurrell, J. W., Hack, J. J., Shea, D., Caron, J. M., Rosinski, J., … Marshall, S. (2008). A New Sea surface temperature and sea ice boundary dataset for the community atmosphere model. *Journal of Climate*, *21*(19), 5145–5153. https://doi.org/10.1175/2008jcli2292.1

Hurrell, J. W., Holland, M. M., Gent, P. R., Ghan, S., Kay, J. E., & Kushner, P. J. (2013). The community earth system model: A framework for collaborative research. *Bulletin of the American Meteorological Society*, *94*(9), 1339–1360. https://doi.org/10.1175/BAMS-D-12-00121.1

Iacono, M. J., Delamere, J. S., Mlawer, E. J., Shephard, M. W., Clough, S. A., & Collins, W. D. (2008). Radiative forcing by long-lived greenhouse gases: Calculations with the AER radiative transfer models. *Journal of Geophysical Research*, *113*, D13103. https://doi.org/10.1029/2008JD009944

Lamarque, J. F., Bond, T. C., Eyring, V., Granier, C., Heil, A., Klimont, Z., … Vuuren, D. P. (2010). Historical (1850–2000) gridded anthropogenic and biomass burning emissions of reactive gases and aerosols: Methodology and application. *Atmospheric Chemistry and Physics*, *10*(15), 7017–7039. https://doi.org/10.5194/acp-10-7017-2010

Laprise, R., de Elía, R., Caya, D., Biner, S., Lucas-Picher, P., Diaconescu, E., … Separovic, L. (2008). Challenging some tenets of regional climate modelling. *Meteorology and Atmospheric Physics*, *100*(1-4), 3–22. https://doi.org/10.1007/s00703-008-0292-9

Lareau, N. P., Crosman, E., Whiteman, C. D., Horel, J. D., Hoch, S. W., Brown, W. O. J., & Horst, T. W. (2013). The persistent cold-air pool study. *Bulletin of the American Meteorological Society*, *94*(1), 51–63. https://doi.org/10.1175/bams-d-11-00255.1

Lauritzen, P. H., Bacmeister, J. T., Callaghan, P. F., & Taylor, M. A. (2015). NCAR_Topo (v1.0): NCAR global model topography generation software for unstructured grids. *Geoscientific Model Development*, *8*(12), 3975–3986. https://doi.org/10.5194/gmd-8-3975-2015

Leung, L. R., & Qian, Y. (2003). The sensitivity of precipitation and snowpack simulations to model resolution via nesting in regions of complex terrain. *Journal of Hydrometeorology*, *4*(6), 1025–1043. https://doi.org/10.1175/1525-7541(2003)004%3C1025:tsopas%3E2.0.co;2

Leung, L. R., Qian, Y., & Bian, X. (2003). Hydroclimate of the western United States based on observations and regional climate simulation of 1981–2000. Part I: Seasonal statistics. *Journal of Climate*, *16*(12), 1892–1911. https://doi.org/10.1175/1520-0442(2003)016%3C1892:hotwus%3E2.0.co;2

Liu, X., Easter, R. C., Ghan, S. J., Zaveri, R., Rasch, P., Shi, X., … Mitchell, D. (2012). Toward a minimal representation of aerosols in climate models: Description and evaluation in the community atmosphere model CAM5. *Geoscientific Model Development*, *5*(3), 709–739. https://doi.org/10.5194/gmd-5-709-2012

Lucas-Picher, P., Laprise, R., & Winger, K. (2017). Evidence of added value in North American regional climate model hindcast simulations using ever-increasing horizontal resolutions. *Climate Dynamics*, *48*(7-8), 2611–2633. https://doi.org/10.1007/s00382-016-3227-z

Martynov, A., Laprise, R., Sushama, L., Winger, K., Šeparović, L., & Dugas, B. (2013). Reanalysis-driven climate simulation over CORDEX North America domain using the Canadian regional climate model, version 5: Model performance evaluation. *Climate Dynamics*, *41*(11–12), 2973–3005. https://doi.org/10.1007/s00382-013-1778-9

McCabe, G. J., Hay, L. E., & Clark, M. P. (2007). Rain-on-snow events in the western United States. *Bulletin of the American Meteorological Society*, *88*(3), 319–328. https://doi.org/10.1175/bams-88-3-319

Mesinger, F., DiMego, G., Kalnay, E., Mitchell, K., Shafran, P. C., & Ebisuzaki, W. (2006). North American regional reanalysis. *Bulletin of the American Meteorological Society*, *87*(3), 343–360. https://doi.org/10.1175/bams-87-3-343

Morrison, H., & Gettelman, A. (2008). A new two-moment bulk stratiform cloud microphysics scheme in the Community Atmosphere Model, version 3 (CAM3). Part I: Description and numerical tests. *Journal of Climate*, *21*(15), 3642–3659. https://doi.org/10.1175/2008JCLI2105.1

National Research Council (2012). *A National Strategy for Advancing Climate Modeling*. Washington, DC: The National Academies Press. https://doi.org/10.17226/13430

Neale, R. B., Richter, J. H., Conley, A. J., Park, S., Lauritzen, P. H., Gettelman, A., … Lin, S.-J. (2010). Description of the NCAR Community Atmosphere Model (CAM5) (NCAR Tech. Note. NCAR/TN-485+STR). Boulder, CO: National Center for Atmospheric Research.

Niu, G.-Y., & Yang, Z.-L. (2007). An observation-based formulation of snow cover fraction and its evaluation over large North American river basins. *Journal of Geophysical Research*, *112*, D21101. https://doi.org/10.1029/2007JD008674

Oleson, K. W., Lawrence, D. M., Gordon, B., Flanner, M. G., Kluzek, E., Peter, J., … Feddema, J. (2010). Technical description of version 4.0 of the Community Land Model (CLM) (NCAR Tech. Note NCAR/TN-4781STR). Boulder, CO: National Center for Atmospheric Research.

Park, S., & Bretherton, C. S. (2009). The University of Washington Shallow Convection and moist turbulence schemes and their impact on climate simulations with the Community Atmosphere Model. *Journal of Climate*, *22*(12), 3449–3469. https://doi.org/10.1175/2008JCLI2557.1

Park, S., Bretherton, C. S., & Rasch, P. J. (2014). Integrating cloud processes in the Community Atmosphere Model, version 5. *Journal of Climate*, *27*(18), 6821–6856. https://doi.org/10.1175/JCLI-D-14-00087.1

Pederson, G. T., Gray, S. T., Woodhouse, C. A., Betancourt, J. L., Fagre, D. B., Littell, J. S., … Graumlich, L. J. (2011). The unusual nature of recent snowpack declines in the North American Cordillera. *Science*, *333*(6,040), 332–335. https://doi.org/10.1126/science.1201570

Rasmussen, R., Baker, B., Kochendorfer, J., Meyers, T., Landolt, S., Fischer, A. P., … Gutmann, E. (2012). How well are we measuring snow: The NOAA/FAA/NCAR winter precipitation test bed. *Bulletin of the American Meteorological Society*, *93*(6), 811–829. https://doi.org/10.1175/bams-d-11-00052.1

Rasmussen, R., Liu, C., Ikeda, K., Gochis, D., Yates, D., Chen, F., … Gutmann, E. (2011). High-resolution coupled climate runoff simulations of seasonal snowfall over Colorado: A process study of current and warmer climate. *Journal of Climate*, *24*(12), 3015–3048. https://doi.org/10.1175/2010jcli3985.1

Rhoades, A. M., Huang, X., Ullrich, P. A., & Zarzycki, C. M. (2016). Characterizing Sierra Nevada snowpack using variable-resolution CESM. *Journal of Applied Meteorology and Climatology*, *55*(1), 173–196. https://doi.org/10.1175/jamc-d-15-0156.1

Rhoades, A. M., Ullrich, P. A., & Zarzycki, C. M. (2017). Projecting 21st century snowpack trends in western USA mountains using variable-resolution CESM. *Climate Dynamics*, 1–28. https://doi.org/10.1007/s00382-017-3606-0

Richter, J. H., & Rasch, P. J. (2008). Effects of convective momentum transport on the atmospheric circulation in the Community Atmosphere Model, version 3. *Journal of Climate*, *21*(7), 1487–1499. https://doi.org/10.1175/2007JCLI1789.1

Sakaguchi, K., Leung, L. R., Zhao, C., Yang, Q., Lu, J., Hagos, S., … Lauritzen, P. H. (2015). Exploring a multiresolution approach using AMIP simulations. *Journal of Climate*, *28*(14), 5549–5574. https://doi.org/10.1175/jcli-d-14-00729.1

Šeparović, L., Alexandru, A., Laprise, R., Martynov, A., Sushama, L., Winger, K., … Valin, M. (2013). Present climate and climate change over North America as simulated by the fifth-generation Canadian regional climate model. *Climate Dynamics*, *41*(11-12), 3167–3201. https://doi.org/10.1007/s00382-013-1737-5

Serreze, M. C., Clark, M. P., Armstrong, R. L., McGinnis, D. A., & Pulwarty, R. S. (1999). Characteristics of the western United States snowpack from snowpack telemetry (SNOTEL) data. *Water Resources Research*, *35*(7), 2145–2160. https://doi.org/10.1029/1999WR900090

Singh, D., Tsiang, M., Rajaratnam, B., & Diffenbaugh, N. S. (2013). Precipitation extremes over the continental United States in a transient, high-resolution, ensemble climate model experiment. *Journal of Geophysical Research: Atmospheres*, *118*, 7063–7086. https://doi.org/10.1002/jgrd.50543

Slingo, J., Bates, K., Nikiforakis, N., Piggott, M., Roberts, M., Shaffrey, L., & Weller, H. (2009). Developing the next-generation climate system models: Challenges and achievements. *Philosophical Transactions of the Royal Society of London, Series A: Mathematical, Physical and Engineering Sciences*, *367*(1890), 815–831. https://doi.org/10.1098/rsta.2008.0207

Ullrich, P. A. (2014). SQuadGen: Spherical quadrilateral grid generator. University of California, Davis, Climate and Global Change Group software. Retrieved from https://github.com/ClimateGlobalChange/squadgen

Verseghy, D. (2009). CLASS—The Canadian land surface scheme (version 3.4)—Technical documentation (version 1.1). Internal report, Climate Research Division, Science and Technology Branch, Environment Canada, p 183.

Walker, M. D., & Diffenbaugh, N. S. (2009). Evaluation of high-resolution simulations of daily-scale temperature and precipitation over the United States. *Climate Dynamics*, *33*(7–8), 1131–1147. https://doi.org/10.1007/s00382-009-0603-y

Walko, R. L., & Avissar, R. (2011). A direct method for constructing refined regions in unstructured conforming triangular–hexagonal computational grids: Application to OLAM. *Monthly Weather Review*, *139*(12), 3923–3937. https://doi.org/10.1175/mwr-d-11-00021.1

Wang, S.-Y., Gillies, R. R., Takle, E. S., & Gutowski, W. J. (2009). Evaluation of precipitation in the intermountain region as simulated by the NARCCAP regional climate models. *Geophysical Research Letters*, *36*, L11704. https://doi.org/10.1029/2009GL037930

Warner, T. T., Peterson, R. A., & Treadon, R. E. (1997). A tutorial on lateral boundary conditions as a basic and potentially serious limitation to regional numerical weather prediction. *Bulletin of the American Meteorological Society*, *78*(11), 2599–2617. https://doi.org/10.1175/1520-0477(1997)078%3C2599:atolbc%3E2.0.co;2

Wehner, M. (2010). Sources of uncertainty in the extreme value statistics of climate data. *Extremes*, *13*(2), 205–217. https://doi.org/10.1007/s10687-010-0105-7

Wehner, M. F. (2013). Very extreme seasonal precipitation in the NARCCAP ensemble: Model performance and projections. *Climate Dynamics*, *40*(1–2), 59–80. https://doi.org/10.1007/s00382-012-1393-1

Williamson, D. L. (2008). Convergence of aqua-planet simulations with increasing resolution in the Community Atmospheric Model, version 3. *Tellus A*, *60*(5), 848–862. https://doi.org/10.1111/j.1600-0870.2008.00339.x

Xie, X., & Zhang, M. (2015). Scale-aware parameterization of liquid cloud inhomogeneity and its impact on simulated climate in CESM. *Journal of Geophysical Research: Atmospheres*, *120*(16), 8359–8371. https://doi.org/10.1002/2015JD023565

Yang, D., Goodison, B. E., Metcalfe, J. R., Golubev, V. S., Bates, R., Pangburn, T., & Hanson, C. L. (1998). Accuracy of NWS 8 standard nonrecording precipitation gauge: Results and application of WMO intercomparison. *Journal of Atmospheric and Oceanic Technology*, *15*(1), 54–68. https://doi.org/10.1175/1520-0426(1998)015%3C0054:aonsnp%3E2.0.co;2

Zadra, A., Caya, D., Côté, J., Dugas, B., Jones, C., Laprise, R., … Caron, L.-P. (2008). The next Canadian regional climate model. *Physics in Canada*, *64*, 75–83.

Zarzycki, C. M., & Jablonowski, C. (2014). A multidecadal simulation of Atlantic tropical cyclones using a variable-resolution global atmospheric general circulation model. *Journal of Advances in Modeling Earth Systems*, *6*(3), 805–828. https://doi.org/10.1002/2014MS000352

Zarzycki, C. M., Jablonowski, C., & Taylor, M. A. (2014). Using variable-resolution meshes to model tropical cyclones in the Community Atmosphere Model. *Monthly Weather Review*, *142*(3), 1221–1239. https://doi.org/10.1175/mwr-d-13-00179.1

Zarzycki, C. M., Jablonowski, C., Thatcher, D. R., & Taylor, M. A. (2015). Effects of localized grid refinement on the general circulation and climatology in the Community Atmosphere Model. *Journal of Climate*, *28*(7), 2777–2803. https://doi.org/10.1175/jcli-d-14-00599.1

Zarzycki, C. M., Levy, M. N., Jablonowski, C., Overfelt, J. R., Taylor, M. A., & Ullrich, P. A. (2014). Aquaplanet experiments using CAM's variable-resolution dynamical core. *Journal of Climate*, *27*(14), 5481–5503. https://doi.org/10.1175/jcli-d-14-00004.1

Zhang, G. J., & McFarlane, N. A. (1995). Sensitivity of climate simulations to the parameterization of cumulus convection in the Canadian Climate Centre general circulation model. *Atmosphere-Ocean*, *33*(3), 407–446. https://doi.org/10.1080/07055900.1995.9649539